INSTITUTE OF NATURAL AND APPLIED SCIENCES
UNIVERSITY OF ÇUKUROVA

Ph.D. THESIS

Mustafa Numan BAKIRCI

CALIBRATION AND TEST STUDIES OF HADRONIC FORWARD, HADRONIC BARREL AND CASTOR DETECTORS AT CMS

DEPARTMENT OF PHYSICS

ADANA, 2009

INSTITUTE OF NATURAL AND APPLIED SCIENCES
UNIVERSITY OF ÇUKUROVA

CALIBRATION AND TEST STUDIES OF HADRONIC FORWARD, HADRONIC BARREL AND CASTOR DETECTORS AT CMS

By Mustafa Numan BAKIRCI

A THESIS OF DOCTOR OF PHILOSOPHY
DEPARTMENT OF PHYSICS

We certify that the thesis titled above was reviewed and approved for the award of degree of the Doctor of Philosophy by the board of jury on ....

Signature............................
Prof. Dr. Gülsen ÖNENGÜT
SUPERVISOR

Signature............................
Prof. Dr. Ayşe POLATÖZ
MEMBER

Signature............................
Assoc. Prof. Dr. İsa DUMANOĞLU
MEMBER

Signature............................
Assoc. Prof. Dr. Ali HAVARE
MEMBER

Signature............................
Assist. Prof. Dr. Turgay İBRİKÇİ
MEMBER

This Ph.D. Thesis is performed in Department of Physics of Institute of Natural and Applied Sciences of Çukurova University
Registration Number:

Prof. Dr. İlhami YEĞİNGİL
Director
The Institute of Natural and Applied Sciences

ÇUKUROVA ÜNİVERSİTESİ

FEN BİLİMLERİ ENSTİTÜSÜ

CMS'TEKİ HADRONİK İLERİ, HADRONİK FIÇI VE CASTOR

DEDEKTÖRLERİNİN KALİBRASYON VE TEST ÇALIŞMALARI

Mustafa Numan BAKIRCI

DOKTORA TEZİ

FİZİK ANABİLİM DALI

Bu tez .... tarihinde aşağıdaki jüri üyeleri tarafından oybirliği/oyçokluğu ile kabul edilmiştir.

İmza............................
Prof. Dr. Gülsen ÖNENGÜT
DANIŞMAN

İmza............................
Prof. Dr. Ayşe POLATÖZ
ÜYE

İmza............................
Doç. Dr. İsa DUMANOĞLU
ÜYE

İmza............................
Doç. Dr. Ali HAVARE
ÜYE

İmza............................
Yrd. Doç. Dr. Turgay İBRİKÇİ
ÜYE

Bu tez Enstitümüz Fizik Anabilim Dalında hazırlanmıştır.
Kod No:

Prof. Dr. İlhami YEĞİNGİL
Enstitü Müdürü
İmza ve Mühür

Not: Bu tezde kullanılan özgün ve başka kaynaktan yapılan bildirişlerin, çizelge, şekil ve fotoğrafların kaynak gösterilmeden kullanımı, 5846 sayılı Fikir ve Sanat Eserleri Kanunundaki hükümlere tabidir.

Sevgili Annem Rahile ve Babam Fehmi'ye...

ABSTRACT

PhD THESIS

CALIBRATION AND TEST STUDIES OF HADRONIC FORWARD, HADRONIC BARREL AND CASTOR DETECTORS AT CMS

Mustafa Numan BAKIRCI

DEPARTMENT OF PHYSICS
INSTITUTE OF NATURAL AND APPLIED SCIENCES
UNIVERSITY OF ÇUKUROVA

In a detector exposed to high flux of particles using optical elements one has to know the level of radiation accumulated to calibrate the optical read-out. At the nominal LHC luminosity the dose received by the fibers at $\eta = 5$ where HF is placed on CMS detector, will be of 100 Mrad/year. In HF the spectrum of Cerenkov light detected by the PMT's is centered near 450 nm (blue). The important light transmission variations at this wavelength due to radiation damage and the fast recovery of it after radiation stops, led us to monitor online the blue light transmission with dedicated fibers called "Raddam fibres". Injecting blue light in a 2.5m long fibre, we used the ratio of the reflected signal at both ends to determine the absorption of the fibre. During the 2006 Raddam device beam test, radiation damage and recovery studies of raddam fibers were performed using LHC-HCAL data acquisition (DAQ).

Results of the performance of the second prototype of the CASTOR quartz-tungsten sampling calorimeter, to be installed in the very forward region of the CMS experiment at the LHC is also discussed in detail. The spatial resolution of the prototype to electromagnetic showers with $E = 100$ GeV electrons from beam tests carried out at CERN/SPS in 2004 using avalanche photodiodes APDs are studied.

Calibrating and testing Hadron Calorimeter (HCAL) components with cosmic-ray muons is a way for improving our understanding of the detector. The SATOCRICH project (Special Assignment to Observe Cosmic Rays in CMS HCAL) proposed to collect and analyze the first sample of cosmic-ray events for CMS HCAL. The experimental setup and results on energy and time distributions of observed cosmic-ray muon events are described. Using cosmic-ray muons preliminary calibration of energy scale of two HCAL wedges is performed and compared with LED and wire-source data.

Key Words: RADDAM, HF, CASTOR, CMS, LHC.

ÖZ

DOKTORA TEZİ

CMS'TEKİ HADRONİK İLERİ, HADRONİK FIÇI VE CASTOR
DEDEKTÖRLERİNİN KALİBRASYON VE TEST ÇALIŞMALARI

Mustafa Numan BAKIRCI

ÇUKUROVA ÜNİVERSİTESİ
FEN BİLİMLERİ ENSTİTÜSÜ
FİZİK ANABİLİM DALI

Danışman: Prof. Dr. Gülsen ÖNENGÜT
Yıl: 2009, Sayfa: 60
Jüri: Prof. Dr. Gülsen ÖNENGÜT
Prof. Dr. Ayşe POLATÖZ
Doç. Dr. İsa DUMANOĞLU
Doç. Dr. Ali HAVARE
Yrd. Doç. Dr. Turgay İBRİKÇİ

Yüksek parşacık akısına (100 Mrad ya da daha fazla) maruz kalan ve fiberlerin aktif ortam olarak kullanıldığı bir dedektörün kalibrasyonu için soğurulan radyasyon miktarı bilinmek zorundadır. LHC ışıklığında CMS'teki HF dedektörünün fiberlerinin maruz kalacağı radyasyon miktarı 100 Mrad/yıl'dır. Radyasyon hasarı ve rejenerasyonundan dolayı 450 nm civarındaki ışık iletimindeki değişimleri Raddam fiberleri adı verilen özel fiberler yardımıyla online olarak izlemek mümkündür. Fiber tarafından soğurulan radyasyon miktarını, gönderilen mavi renkli ışığın 2.5 m uzunluğundaki fiberin iki ucundan yansıyan sinyallerin oranından tespit etmek mümkündür. 2006 yılında yapılan demet testi ile raddam fiberlerinin radyasyon hasari ve iyileşme miktarı LHC-HCAL veri edinim sistemi kullanılarak çalışılmıştır.

Ayrıca, LHC deneyindeki CMS dedektörünün ileri kalorimetrelerinden biri olan CASTOR kuartz-tungsten kalorimetresının ikinci prototipinin performans sonuçları detaylıca tartışılmıştır. CERN/SPS'ten elde edilen 100 GeV enerjili elektronlarla kalorimetrenin elektromanyetik duşlara karşı uzaysal çözünürlüğü çığ fotodiyotları (APD) kullanılarak araştırılmıştır.

Son olarak SATOCRICH (Special Assignment to Observe Cosmic Rays in CMS HCAL) projesi ile kompakt müon solenoidinin hadronik kalorimetresinde ilk kozmik müon verileri alınmış ve analiz edilmiştir. Kozmik müonlar yardımıyla CMS hadronik kalorimetrenin altdedektörleri kalibre edilebilir. Deney sistemi ve kozmik müonların enerji ve zamanlama dağılımları açıklanmış ve hadron kalorimetresinin iki sektörünün kozmik müonlar kullanılarak başlangıç kalibrasyon skalası belirlenmiş ve LED ve radyoaktif kaynak verileri ile karşılaştırılması yapılmıştır.

Anahtar Kelimeler: RADDAM, HF, CASTOR, CMS, LHC.

ACKNOWLEDGEMENTS

CONTENTS   **PAGE**

LIST OF TABLES PAGE

LIST OF FIGURES **PAGE**

ABBREVATIONS

ADC	Analog to Digital Converter
ALICE	A Large Ion Collider Experiment
APD	Avalanche Photo Diode
ATLAS	A Toroidal LHC ApparatuS
CASTOR	Centauro And STrange Object Research
CERN	Conceil Europeenne pour la Recherche Nucleaire
CMS	Compact Muon Solenoid
DAQ	Data AcQusition
DCC	Data Concentrator Card
ECAL	Electromagnetic CALorimeter
HCAL	Hadronic Calorimeter
HF	Hadronic Forward
HPD	Hybrid Photo Diode
HTR	HCAL Trigger/Readout Board
IRRAD	CERN irradiation facilities
LEP	Large Electron Positron Collider
LHC	Large Hadron Collider
LHC-b	Large Hadron Collider Beauty Experiment
QCD	Quantum ChromoDynamics
QED	Quantum ElectroDynamics
QIE	Charge Integrator
RADDAM	RADiation DAmage Online Monitoring
RBX	Readout BoX
PMT	Photo Multiplier Tube
SATOCRICH	Special Assignment to Observe Cosmic Rays In CMS HCAL
SHLC	Super LHC
SM	Standard Model
SUSY	SUper SYmetry

TEC   Tracker End Cap

TIB   Tracker Inner Barrel

TID   Tracker Inner Disk

TOB   Tracker Outer Barrel

TTC   Timing, Triggering and Control

TS   Time Slice

UHE   Ultra High Energy

VBF   Vecto Boson Fusion

ZDC   Zero Degree Calorimeter

1. INTRODUCTION

Particle physics which is also called high energy physics investigates matter, it's constituents and interactions between them. Since mid-20th century various experiments were carried out and their results constructed our knowledge of structure of matter. The elementary particles and their fundamental interactions are well described by the **S**tandard **M**odel (SM). According to the SM all visible matter in the Universe is made up of fermions which have spin $\frac{1}{2}$. There are 12 funamental fermions and their corresponding antiparticles. The fundamental fermions are classified as quarks and leptons according the charges their interactions. There are six quarks (up, down, charm, strange, top and bottom) and six leptons (electron, muon, tau and corresponding neutrinos). The quarks, leptons and their antiparticles are subdivided into three generations (see Table 1.1.).

Table 1.1. The 12 fundamental fermionic particles and their antiparticles

First generation		*Second generation*		*Third generation*	
Leptons					
Name	*Symbol*	*Name*	*Symbol*	*Name*	*Symbol*
electron	e^-	muon	μ^-	tau	τ^-
electron neutrino	ν_e	muon neutrino	ν_μ	tau neutrino	ν_τ
Quarks					
up quark	u	charm quark	c	top quark	t
down quark	d	strange quark	s	bottom quark	b
Antileptons					
antielectron	e^+	antimuon	μ^+	antitau	τ^+
electron antineutrino	$\overline{\nu_e}$	muon antineutrino	$\overline{\nu_\mu}$	tau antineutrino	$\overline{\nu_\tau}$
Antiquarks					
up antiquark	$\overline{u}$	charm antiquark	$\overline{c}$	top antiquark	$\overline{t}$
down antiquark	$\overline{d}$	strange antiquark	$\overline{s}$	bottom antiquark	$\overline{b}$

There are four fundamental forces (electromagnetic, weak, strong and gravitational) which are carried by *force mediating particles* called 'bosons' that are responsible for the interactions between the fermions. The bosons have spin 1 and are described as following:

1. The electromagnetic force is mediated by massless photons between electrically charged particles. Quantum electrodynamics (QED) describes the electromagnetic interactions by photon exchange.

2. The weak interactions between all quarks and leptons are mediated by massive W^+, W^- and Z gauge bosons. The W^+ and W^- bosons carry electric charge +1 and -1 respectively whereas Z is electrically neutral. The weak is force responsible for some nuclear reactions like beta decay.

3. The strong force mediated by eight massless gluons (g) between the color charged particles (the quarks). The strong force also binds atomic nuclei together and make them stable. The interactions of the quarks and gluons making up hadrons are described by Quantum chromodynamics (QCD). Strong force combines quarks into two types of bound states: baryons (qqq states) and mesons ($q\bar{q}$ states).

4. The gravitational force is mediated by a hypothetical elementary particle called graviton in the framework of quantum field theory. The graviton is assumed to be massless because the gravitational force has unlimited range. Gravitational force is negligible between the fundamental fermions, because their masses are very small (see Figure 1.1.).

Quarks interact through all the other three interactions: strong, weak and electromagnetic. Charged leptons interact through electromagnetic and weak interactions and neutrino interact only weakly.

Figure 1.1.   Elementary particles in Stadard Model

There is no contradiction observed experimentally with the SM so far but since gravity can not be included in to the SM, it can be regarded as an uncomplete theory of fundamental interactions. Furthermore, altough SM describes the subatomic world well, there are several open questions that SM that is inadequate to answer like:

- Are there only three families of quarks and leptons?

- What is dark matter?

- What happened to the missing antimatter?

- Where does the different masses of all fermions come from?

- Are the SM fundamental particles really fundamental?

A theoretical explanation introduced by P. Higgs in 1964 suggests that the masses of the fundamental particles are generated through the interaction with a massive scalar elementary particle called Higgs (Higgs, 1964). It has no intrinsic spin, thus, it is classified as a boson. Altough the Higgs boson which is the key to the origin and essential ingredient of particle masses has not been found in any experiment yet there is a lower limit in Higgs boson production at 114.4 Gev/c^2 for a 95% CL introduced by direct searches at LEP (The LEP Working Group for Higgs Boson Searches, 2003). The combined results from CDF and D0 on direct searches for a SM Higgs boson (H) in $p\bar{p}$ collisions at the Fermilab Tevatron excluded recently the mass range of SM Higgs extending to $160 < m_H < 170 \, \mathrm{GeV/c^2}$ for a 95% C.L. (The TEVNPH Working Group, 2009). It is hoped that the Large Hadron Collider (LHC) at CERN will confirm the existence of Higgs particle in TeV scale with it's extraordinary electronic eyes and also provide answers to the questions about SM.

In the 2nd chapter of this thesis short information will be given about LHC and the CMS experiment which is one of two general purpose experiments on LHC aiming to observe Higgs boson and discover new physics beyond SM. The following three chapters describe three different contributions to the CMS experiment by the author:

1. radiation damage and recovery studies of the hadronic forward calorimeter (HF)

2. beam test studies of 2nd prototype of the CASTOR calorimeter

3. calibration of hadronic calorimeter (HCAL) with cosmic muons

2. THE LHC AND CMS EXPERIMENT

2.1   The Large Hadron Collider(LHC)

The Large Hadron Collider (LHC) has been constructed at CERN in Geneva, Switzerland. It is the largest hadron collider in the world ever built. First engineering runs began in 10 September 2008. But, on 19 September 2008, during the *without beam* commissioning of the sectors 3-4 at high current for operation at 5 TeV, an incident occurred caused by a faulty electrical connection between two magnets resulting in a large helium leak into the tunnel. Since than experts have been working on it to get the first collisions in fall 2009. The proton-proton collisions will be at a centre-of-mass energy $\sqrt{s} = 14$ TeV in 27 km circumference tunnel underneath the French-Swiss border. But the centre-of-mass energy will be $\sqrt{s} = 10$ TeV for the first year. The aerial view of LHC can be seen in Figure 2.1.

Figure 2.1.   The aerial view of LHC

The existing CERN facilities has been upgraded to provide the pre-accelerated protons for LHC. There are a series of existing machines which will be used to accelerate the protons to high energies; a Linac will bring them up to 50 MeV, a Booster up to 1.4 GeV,

the PS up to 25 GeV and SPS up to 450 GeV, finally they will enter to LHC which is going to take them up to 7 TeV. Figure 2.2. shows the series of CERN accelerator machines.
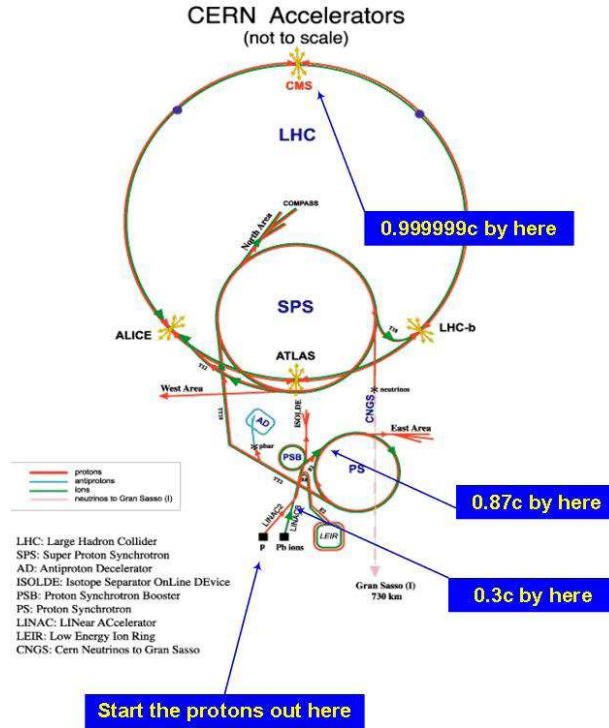
Figure 2.2.   CERN accelerators

Proton bunches will collide at 40 MHz frequency, or every 25 ns. These bunches will have transverse spread $\sigma_x = \sigma_y = 15$ μm and longitudinal spread 7.5 cm at the collision. The rate of a physics process can be calculated by

$$R = \sigma L \tag{2.1}$$

where σ is the cross section and L is luminosity. The accelerator luminosity can be obtained by

$$L = \frac{f n_1 n_2}{4\pi \sigma_1 \sigma_2} \tag{2.2}$$

where n_1 and n_2 are the number of particles in the bunches and f is collision frequency.

The design luminosity of LHC is expected to reach $\mathcal{L} = 10^{34}$ cm^{-2}s^{-1}, that is about 100 times more than the current luminosities reached by existing colliders in the world and

this *high luminosity* will allow to collect approximately 100 fb^{-1} per year. LHC is planned to run at *low luminosity* of $\mathcal{L} = 2 \times 10^{33}$cm^{-2}s^{-1} for the first three years and collect an estimated 10 fb^{-1} per year for this period. In addition to proton-proton collisions, LHC will provide heavy ion (lead) collisions with a centre-of-mass energy of 2.76 TeV per nucleon. This energy level is about 30 times higher than the Relativistic Heavy Ion Collider (RHIC) at the Brookhaven Laboratory (Akgun, 2003). Some LHC parameters can be found in Table 2.1.

Table 2.1.   Some LHC parameters *pp* and *PbPb* collisions)

Parameters	$p-p$	$Pb-Pb$
Center of mass energy (TeV)	14	5.52
Number of bunches	2808	592
Number of particles per bunch	$\sim 10^{11}$	$\sim 5 \times 10^{7}$
Bunch spacing (ns)	25	100
Luminosity (cm^{-2} s^{-1})	10^{34}	10^{27}

In LHC, two separate beam channels with opposite directions are required so as to accommodate collisions between the same types of particles. The new TeV scale physics will be explored by the following experiments at LHC: **C**ompact **M**uon **S**olenoid (CMS), **A** Large **T**orodial **LHC** **A**pparatu**S** (ATLAS), **L**arge **H**adron **C**ollider **b**-quark (LHC-b) and **A** **L**arge **I**on **C**ollider **E**xperiment (ALICE). The CMS and ATLAS are multipurpose detectors both in $p-p$ and $Pb-Pb$ collisions. LHC-b is dedicated for b-physics and ALICE will search quark-gluon plasma (QGP) in PbPb collisions. Schematic layout of LHC can be seen in Figure 2.3.

2.2   The Compact Muon Solenoid (CMS)

In this section, the components of the CMS detector are explained. As a compact multipurpose detector, CMS will explore new physics at TeV scale. At the heart of CMS, a 13 m long, 5.9 m inner diameter superconducting solenoid magnet, largest ever built is placed. It will have $B = 4$T magnetic filed for measuring the momentum of charged particles precisely. The detector is called compact because the tracker, elektromangnetic calorimeter (ECAL) and hadronic calorimeter (HCAL) are placed inside the magnet. To detect muons that might be signatures of interesting events, CMS is surrounded by muon
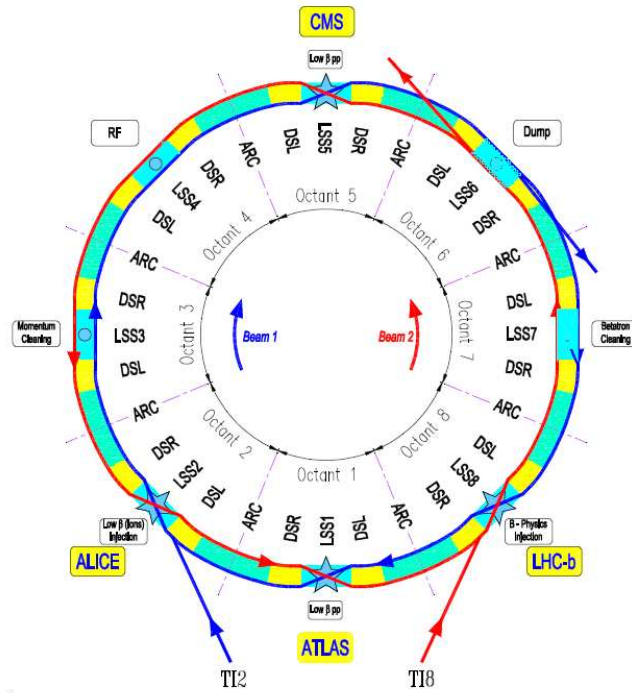
Figure 2.3.   Schematic layout of LHC

dedectors which consist of drift tubes (DT), cathode strip chambers (CSC) and resistive plate chambers (RPC). An overall picture of the CMS can be seen in Figure 2.4. The details of the CMS detector are described below.

2.2.1   The Tracker System

As closest part of the CMS to beam pipe, the CMS tracker system is designed to reconstruct high p_T muons, electrons, and hadrons with high momentum resolution. There are two kind of tracker system is used for CMS. Pixel tracker and strip tracker. The silicon pixels and the silicon strips enable charged particles to be tracked and their momenta to be measured. Figure 2.5. shows the tracking system of CMS.

2.2.1.1   The pixel tracker

The pixel tracker consists of 3 barrel layers which are located at mean radii of 4.4 cm, 7.3 cm and 10.2 cm, and have a length of 53 cm and 2 endcap disks which are placed on each side at $|z|$ = 34.5 cm and 46.5 cm. In order to achieve the optimal vertex
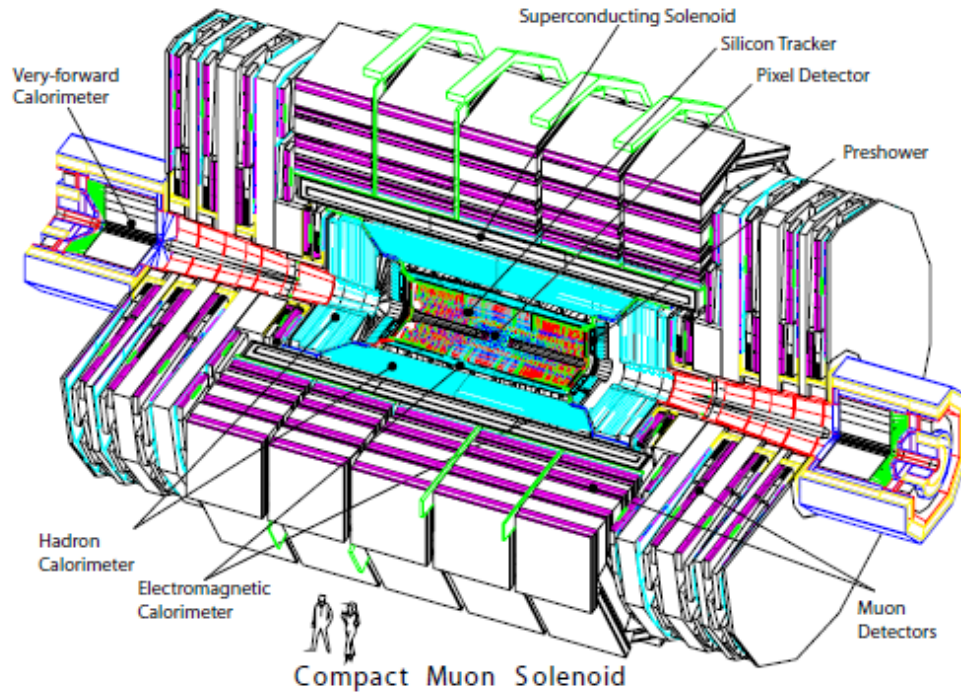
Figure 2.4.   Schematic layout of CMS

position resolution a pixel shape of 100×150 m^2 is used. The barrel consists of 768 pixel modules. The endcap disks consists of 672 turbine-like geometry with blades pixel modules. The barrel pixel detectors cover central region $|\eta| < 1.6$, and endcaps cover the region $|\eta| < 2.5$.

2.2.1.2   The strip tracker

The barrel tracker region is divided into Tracker Inner Barrel (TIB) which has 4 layers covering $|z| < 65$ cm, using silicon sensors with a thickness of 320 m and a strip pitch which varies from 80 to 120 m and a Tracker Outer Barrel (TOB) which has 6 layers with a half-length of $|z| < 110$ cm. The endcaps are divided into two parts which are the Tracker End Cap (TEC) and Tracker Inner Disks (TID). Each TEC comprises 9 disks extending into the region 120 cm$< |z| < 280$ cm, and each TID comprises 3 small disks that fill the gap between the TIB and the TEC The entire silicon strip detector consists of almost 15 400 modules. More information on the tracker can be found at (CMS Collaborion, 1998).
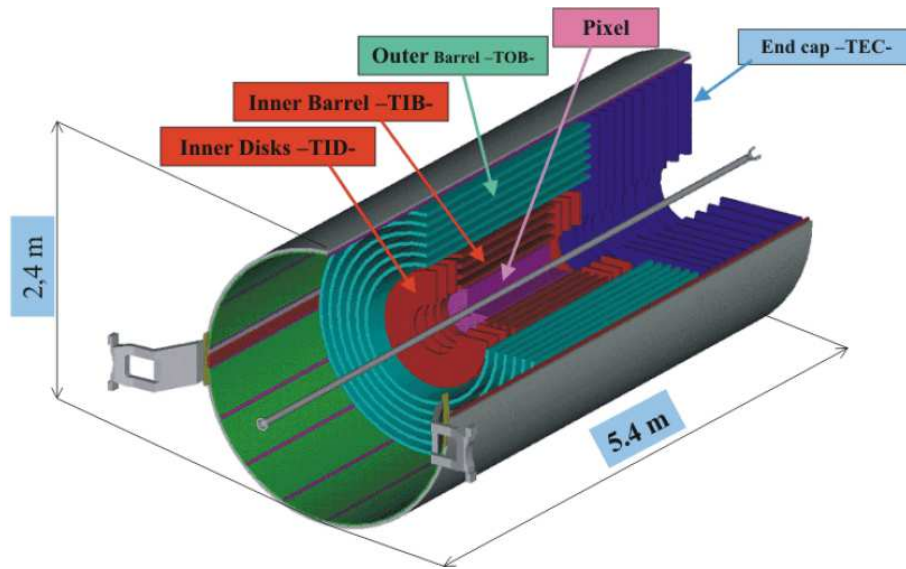
(a)
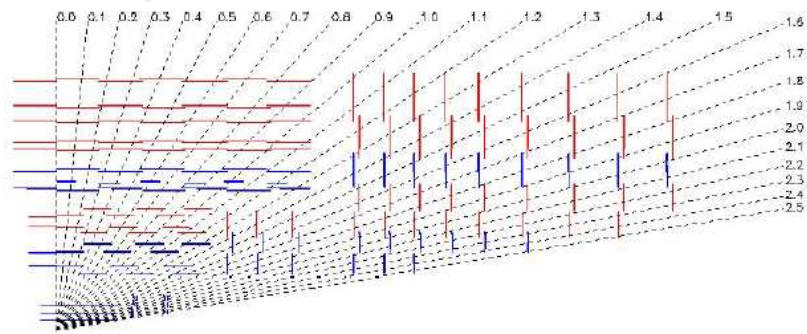
(b)

Figure 2.5.   The muon dedectors (a), The *z* view of muon system (b)

2.2.2   CMS Calorimeter System

In order to measure the energy of jets and missing transverse energy, a hermetic and complete calorimeter system is needed for both electromagnetic and hadronic particles. There are two calorimeter systems used in CMS, Electromagnetic and Hadronic calorimeters.

2.2.2.1   The Electromagnetic Calorimeter (ECAL)

The design purpose of the electromagnetic calorimeter (ECAL) is to measure energies and positions of photons and electrons with high precision. As a homogenous calorimeter ECAL is made of lead tungstate (PbWO4) crystals as active material which have high density (8.2 g/cm^3), short radiation length ($X_0 = 0.89$ cm), and very small Molière radius (RM = 2.19 cm). There are approximately 80000 ECAL crystals with a dimension of 2.2cm$\times$2.2cm$\times$23cm each. The crystals are readout by Avalanche Photo Diodes (APDs) and Vacuum photo triodes (VPTs). There are two parts of ECAL which are the barrel (EB) and the endcap (EE). Figure 2.6. shows the transverse view of ECAL.
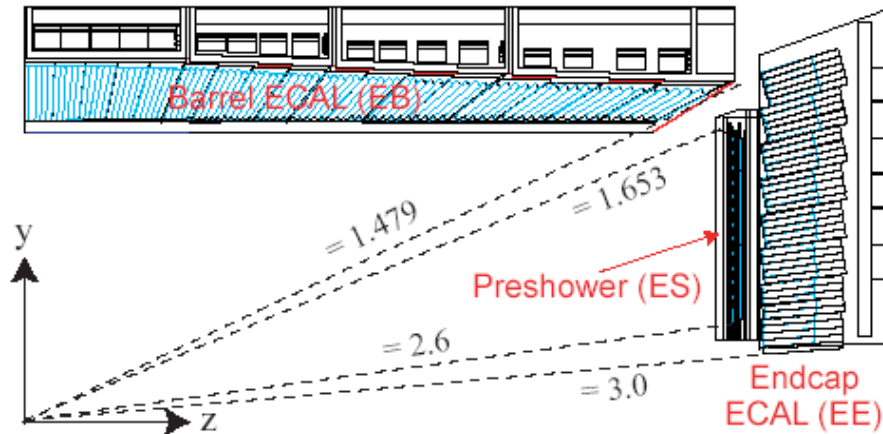
Figure 2.6.   Transverse section through the ECAL, showing geometrical configuration

The 61200 crystals pocked into 36 supermodules. Each supermodule has $5 \times 5 = 25$ crystals. The EB covers the $|\eta| < 1.48$ region. The crystals are readout by APDs. The EE ranges between $1.5 < |\eta| < 3.0$. Each EE is divided into two halves consisting of 3662 crystals each. The EE is readout by Vacuum photo triodes (VPTs). There is a preshower

detector (ES) in front of EE covering the $1.6 < |\eta| < 2.6$ region. The purpose of the preshower detector is to reject π^0s which decay into two closely separated photons in order to reduce one kind of background for the channel, which Higgs boson decays into two photons, by eliminating these π^0s (CMS Collaboration, 1997a).

2.2.2.2   The Hadronic Calorimeter (HCAL)

Together with the ECAL, the hadronic calorimeter (HCAL) is designed to identify hadrons and jets and to measure their energies. HCAL is made of brass layers as absorber interleaved by plastic scintillators as active material. HCAL completely surrounds the ECAL in solenoid magnet. The HCAL consists of barrel (HB), endcap (HE), outer (HO) and forward (HF) detectors. The HB consists of two half barrels and is composed of 18 $20°$ wedges in ϕ covering $|\eta| < 1.4$. HE covers $1.5 < |\eta| < 3.0$ region. HE also has 18-fold ϕ geometry as HB. Since HB is not deep enough to contain a hadronic shower fully, HO is designed to catch the tails of hadronic shower covering the region $|\eta| < 1.26$. Light collected from the scintillators in HB, HE and HO are read out by the Hybrid Photo Diodes (HPD). The schemaic view of HB and HE can be seen in Figure 2.7.
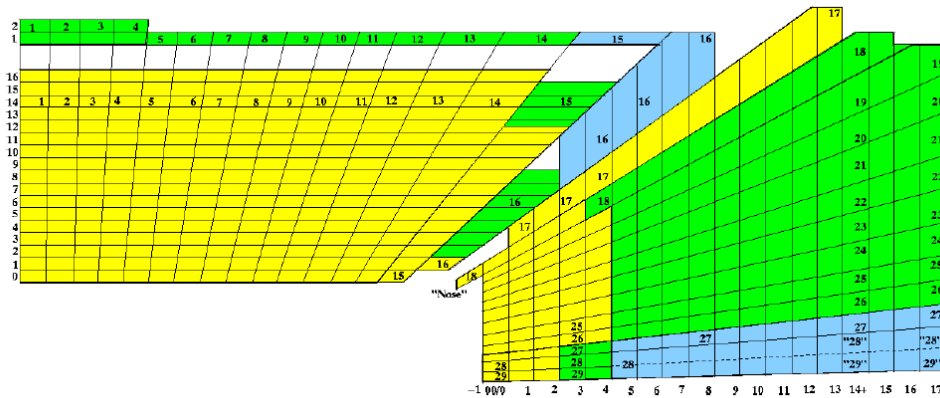
Figure 2.7.   HB and HE schematic view

The HF iron-quartz calorimeters are the forward detectors of HCAL covering the pseudorapitidy region $3.0 < |\eta| < 5.0$. They are located at the two ends of the CMS detector. HF located outside the CMS magnetic coil is made of an iron absorber and quartz fibers as the active medium. Quartz fibers are chosen because they are highly radiation

hard since thay will work in a high radiation environment. HF calorimeters are designed to identify high energy jets with good precision (20% to 30% at 1 TeV) (Abdullin et al., 2008). The radiation damage and recovery measurements of HF's quartz fibers in a PS test beam data are discussed in Chapter 3.

In addition, the CASTOR calorimeter will be placed ±14 m from interaction point (IP) which covers $5.2 \leq |\eta| \leq 6.4$ to study wide range of physics programme in $p-p$, $p-A$ and $A-A$ collisions. More information about HCAL can be found at (CMS Collaboration, 1997b).

2.2.3 The Magnet

The CMS solenoid magnet is designed to produce a four tesla uniform magnetic field by a 20 kA current. The solenoid has a length of 13 m and a radius of 5.9 m. The 4 T magnetic field will contribute information of the reconstruction of transverse momenta of charged particles by bending the tracks. Detailed information about the magnet can be found at (CMS Collaboration, 1997c).

2.2.4 The Muon System

The muon system is designed to find trajectories of muons since they play an important role in interesting physics. Muon system consists of three type of detecetors which are drift tubes (DTs) in the barrel region, cathode strip chambers (CSCs) in the endcap region and resistive plate chambers (RPCs) both in barrel and endcap regions. Four layers of muon detectors are distributed in the barrel and endcap sections of return yoke. The DTs cover $|\eta| < 1.2$ and CSCs cover $1.2|\eta| < 2.4$ region giving a muon vector resolution in $r-\phi$ plane 100 μm and 200 μm respectively. An RPC consists of two graphite-coated bakelite plates forming cathodes interleaved by a gas gap and are operated in avalanche mode giving a time resolution of $\sim$1 ns. A layout of the muon system is given in Figure 2.8.

More information about the muon system can be found at (CMS Collaboration, 1997d).
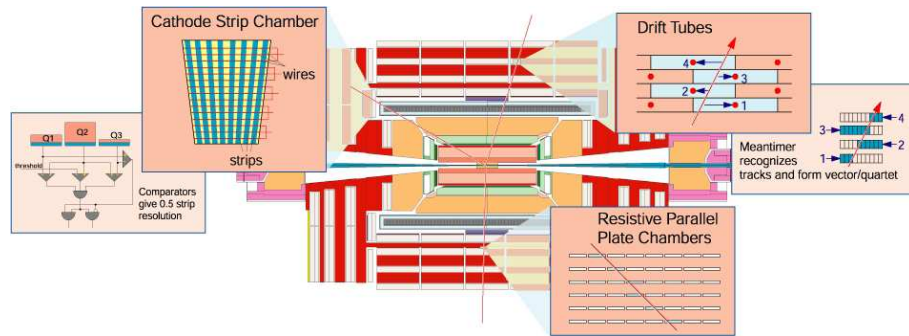
(a)
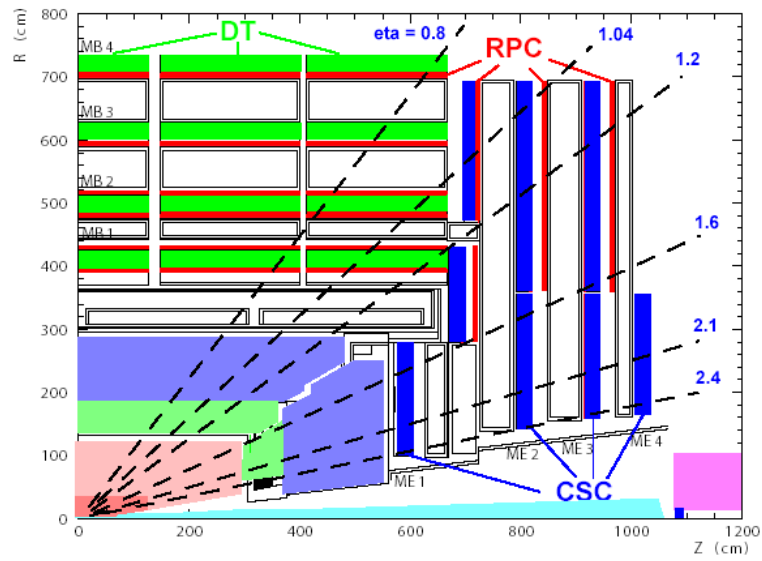
(b)

Figure 2.8.   The muon dedectors (a), Transverse section of muon system(b)

2.2.5   The Trigger
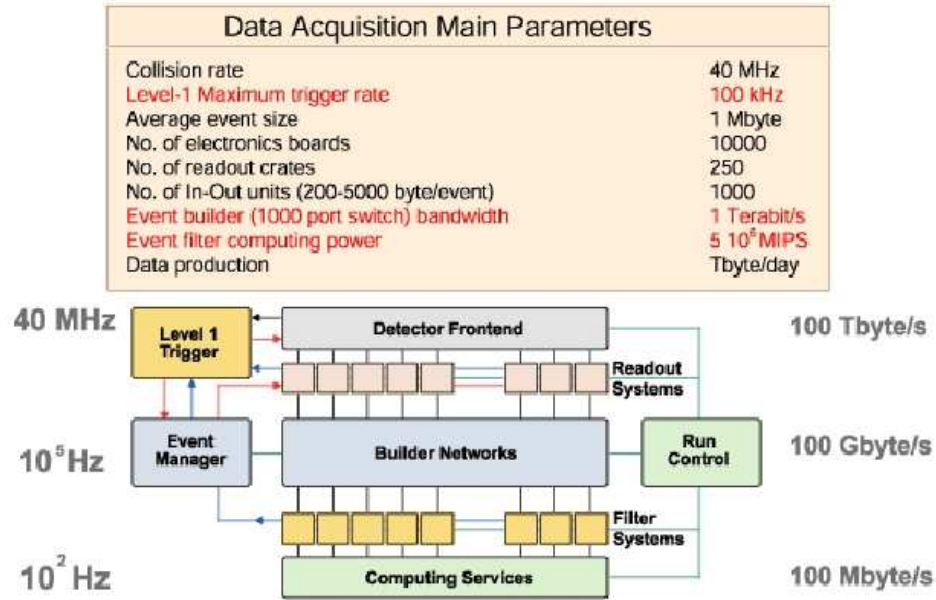
Figure 2.9.   The CMS trigger and data acquisition structure are shown

The LHC will have a bunch crossing rate of 40 MHz leading approximately to 10^9 interactions/sec at the luminosity of $\mathcal{L} = 10^{34}\text{cm}^{-2}\text{s}^{-1}$. Only about 20 crossings data can be written to archival media rejecting factor of nearly 10^6. The CMS trigger system (The TriDAS Project Technical Design Report, 2000) consists of 2 parts which are the Level-1 trigger processors (calorimeter, muon, and global) and an online event filter system (processor farm) that executes the software for the High-Level Triggers (HLT).

The L1 is a hardware trigger which uses the calorimeters and muon system seeking signs of interesting events. The total time for transition from the detectors and for reaching a decision to keep or discard data from a particular beam crossing is 3.2 μs. During this time the data is kept in the buffers for decision of whether or not the data is useful. The average rate for transferring the full detector information to the readout system is 100 kHz.

The HLT reduces the output of L1 trigger rate 100kHz to 100 Hz selecting events by running software on a farm of computer processors. HLT uses information of calorimeter

and muon systems, followed by the use of the tracker pixel data and finally the use of the full event information and completes the particle identification. The trigger and data acquisition system can be seen in Figure 2.9. (CMS Collaboration, 2000; CMS Collaboration, 2002).

2.3   Forward detectors at the CMS

The central CMS has an acceptance in pseudorapidity $|\eta| < 2.5$ for tracking and $|\eta| < 3$ for calorimeter information. In order to enhance forward detection capabilities CMS has several forward detectors which are briefly described below according to CMS/TOTEM TDR, 2006.

The hadron forward calorimeters (HFs) which are iron/quartz-fibre calorimeters placed at ± 11 m from the IP covering $3.0 < |\eta| < 5.0$. The Čerenkov light emitted in the quartz fibres is detected by photomultipliers (Abdullin et al., 2008).

The CASTOR calorimeter which is a quartz-tungsten sampling calorimeter is located at 14 m from the IP and covers the pseudorapitidy of CMS $5.3 < |\eta| < 6.6$. The calorimeter is designed to observe and measure the propagation of hadronic cascades (showers) along its depth using Čherenkov light as in HF (Aslanoglu et. al., 2007).

The Zero Degree Calorimeters (ZDCs) are compact and radiation hard calorimeter as HF, based on Čherenkov light production using tungsten-quartz fiber layers. It is located at 140 m from the IP covering $|\eta| > 8.1$ pseudo rapidity region and can measure the energy deposit of neutral particles (e.g. photons and neutrons)(Grachov et.al., 2006).

The TOTEM forward tracker telescopes T1 ($3.1 < |\eta| < 4.7$) and T2 ($5.2 < |\eta| < 6.5$) are in both sides of CMS, at 7.5 and 14 m respectively. They are optimized to measure the total p-p cross-section and study elastic scattering and diffractive processes at the LHC in dedicated, special-optics runs (Berardi et al., 2004).

The Roman Pots detector system which are ± 220 m and ± 240 m from the IP and are optimized in view of measuring proton scattering angles down to a few rad (Royon, 2007).

FP420 is a magnetic spectrometer proposed to be ± 420 m from the IP. It is designed to define the spatial position as well as the arrival time of the outgoing protons at several points in a 10 m region around 420 m. The displacement (and angle) of the outgoing

protons relative to the beam allows the momentum loss and transverse momentum of the scattered protons to be reconstructed (Albrow et. al., 2009).
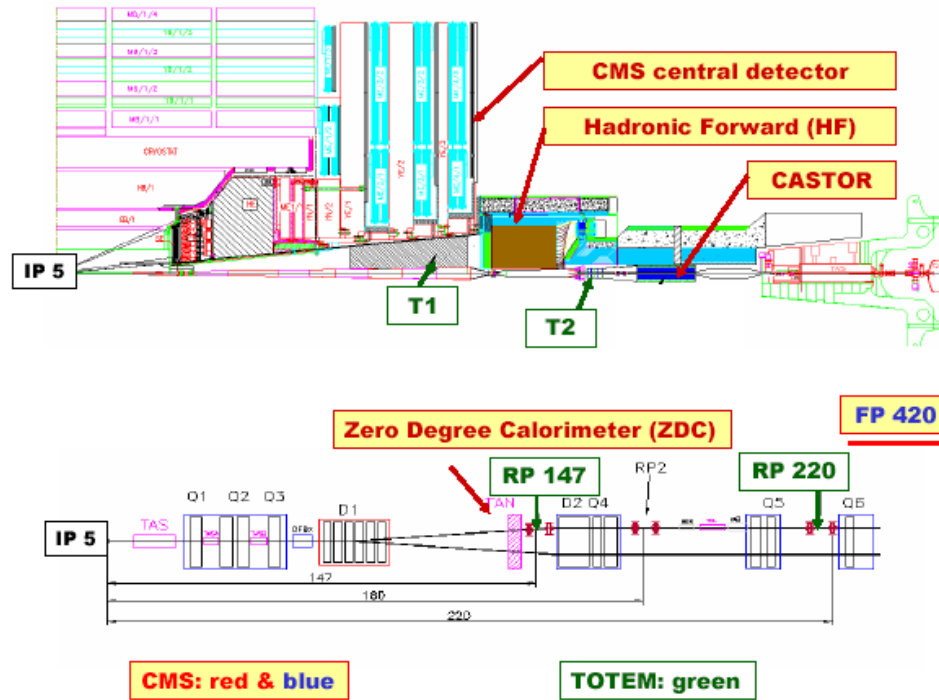
Figure 2.10.   The layout of HF, TOTEM, CASTOR and ZDC forward detectors of CMS

The forward instrumentation can be used for different purposes such as detectors, as tagging devices and as vetoing devices (d'Enterria, 2008). Having an unprecedented coverage of the forward region of CMS, a large variety of physics topics can be studied with these instrumentation. The physics measurements of forward detectors are summarized in the next section.

2.4   Forward Physics at the CMS

The program of forward physics covers a wide range of physics subjects and can be listed as an overview in the following (Borras, 2007):

- Diffraction

    - soft diffraction

- – hard diffraction

- – double pomeron exchange diffraction

- – diffractive Higgs production

- – SUSY

- Low-x dynamics

- Multiparton interactions and underlying event structure

- measurements for validation of Cosmic Ray Physics Model

- Photon - proton and photon - photon physics

- Forward physics in heavy ion collisions

- Photon - proton and photon - photon physics

- Luminosity determination

Being the forward detectors of CMS, HF, CASTOR and ZDC calorimeters together with the TOTEM telescopes, can be seen as probes of new physics studies.

The hadronic models of ultra-high-energy (UHE) cosmic-rays interactions can be effectively tuned by measuring the forward energy and particle flows in $p - p$, $p - A$, and $A - A$ collisions, because the center of mass energy in $p - p$ collisions at the LHC correspond to 100 PeV energy in a fixed target collision which is the energy of cosmic rays, generating extended air shower in proton-nucleus and nucleus-nucleus collisions at upper atmosphere (d'Roeck, 2005).

In hadron-hadron collisions there are not only hard parton-parton collisions but also soft interactions between the partons of the remnants of the beam particles which lead to higher energy level in underlying event that has to be understood and taken into account in the calculations which is important for Higgs production studies. According to generator level studies, the forward region is especially sensitive in energy and mean charged particle flow to the different models for underlying event structure and multi-parton interactions (Borras, 2007).

One of the Higgs production mechanisms at LHC is accompanied by forward particle emission which is called vector-boson-fusion (VBF) process. The Higgs is produced

in $p - p$ collisions by merging of W and Z bosons which are radiated by two valance quarks fragmenting into two forward-backward jets tagged in the forward calorimeters (d'Enterria, 2008).

Moreover, there will be many interesting physics events which are gateway to the answers of the questions that SM cannot deal, and to new physics which can only be detected by the use of these forward detectors.

3. RADIATION DAMAGE and RECOVERY STUDIES

3.1   Introduction

3.1.1   Physics interest of the forward region

Being one of the forward calorimeters of CMS at LHC, HF has an important role in diffractive physics, low-*x* QCD and new physics studies such as top quark production, Standard Model Higgs and SUSY particle searches. Forward detectors are expected to identify high energy quark jets which are important for Higgs boson detection. Covering the pseudorapidity range $3 \leq |\eta| \leq 5$ in the forward region, CMS's jet detection and missing transverse energy resolution are considerably improved by the HF calorimeters.

3.1.2   HF calorimeters

CMS HF calorimeters are Čerenkov effect based calorimeters symmetrically located 11.15m from the interaction point on both sides. Čerenkov radiation opening angle is given by

$$\cos\theta_c = \frac{1}{n\beta} \tag{3.1}$$

where $\beta = v/c$ and n is refractive index of quartz. The total light yield due to the Čerenkov effect is calculated as

$$\frac{d^2N}{dxd\lambda} = 2\pi\alpha z^2(\sin^2\theta_c/\lambda^2) \tag{3.2}$$

where α ($\alpha = \frac{1}{137}$) is the fine structure constant, θ_c is the Čerenkov angle, λ is the wavelength of the emitted light, x is the path of the particle in the medium and z is the charge of the incident particle.

The HF quartz fibers embedded into the iron absorber. The fibers are installed parallel to the beam axis in two different lengths called short (EM,143cm) and long (HAD,165cm) corresponding to EM and HAD parts respectively. The long fibers detect all of the elec-

tromagnetic showers (EM) generated by electrons and photons hitting the front of HF and part of the hadronic showers. The short fibers detect the major part of hadronic showers (HAD). The EM and HAD fibers are readout separately in order to categorize showers which are generated by electrons and hadrons. The radius of the cylindrical HF is 130.0 cm and it is azimuthally subdivided into 18 wedges of 20° each (see Figure 3.1.). The
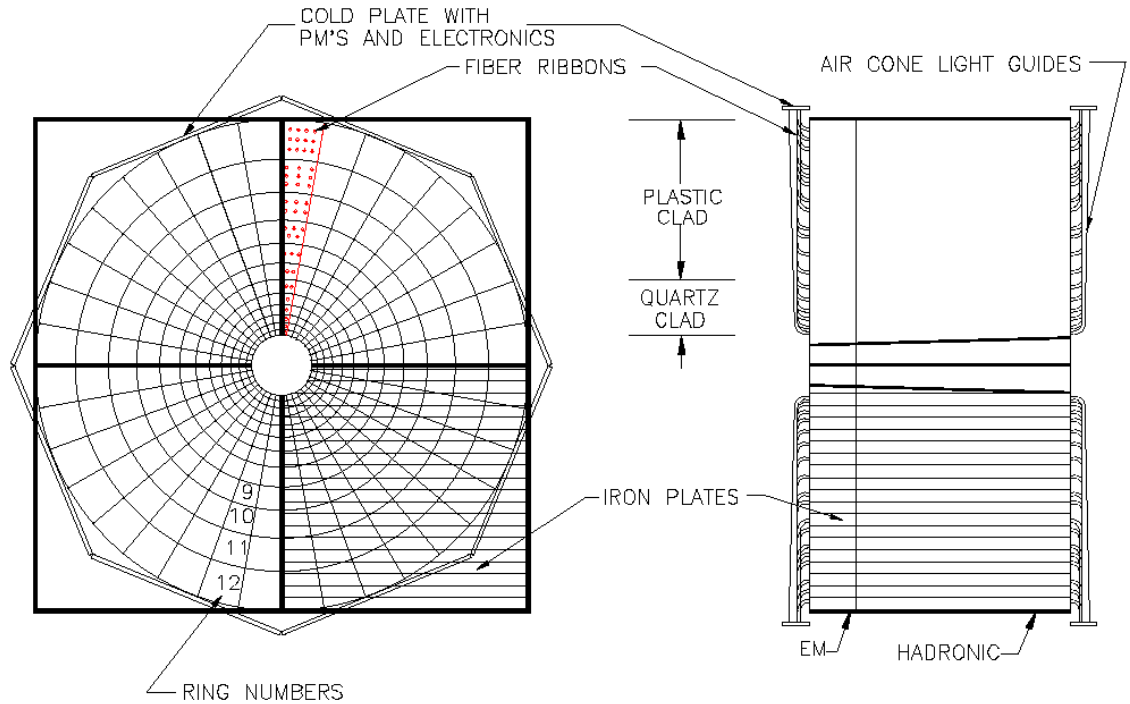
Figure 3.1.   Schematic design drawing of the HF calorimeter

fibers are bundled and readout by a standard bialkaline, 8-stage photomultiplier tube with a borosilicate window[1] which is coupled to air-core light guides covered by metal-coated reflectors inside. There are 24 PMTs in a readout box (RBX) which serves 10° of a wedge that corresponds to half of one wedge (Abdullin et al., 2008). The cross sectional view of HF can be seen in Figure 3.2.

In LHC, protons will collide with 7 TeV energy and an unprecedented peak luminosity of $10^{34} \mathrm{cm}^{-2} \mathrm{s}^{-1}$ in order to get adequate parton-parton interactions which suggest 7×10^8 interactions per second if inelastic *pp* cross section is 70 mb (Huhtinen, 1996). These extremely high particle fluxes will generate sizeable radiation doses which will affect most the forward calorimeters at the highest rapidities. On average, 760 GeV per proton-

---

[1] (R7525) Manufactured by Hamamatsu Photonics, Japan.
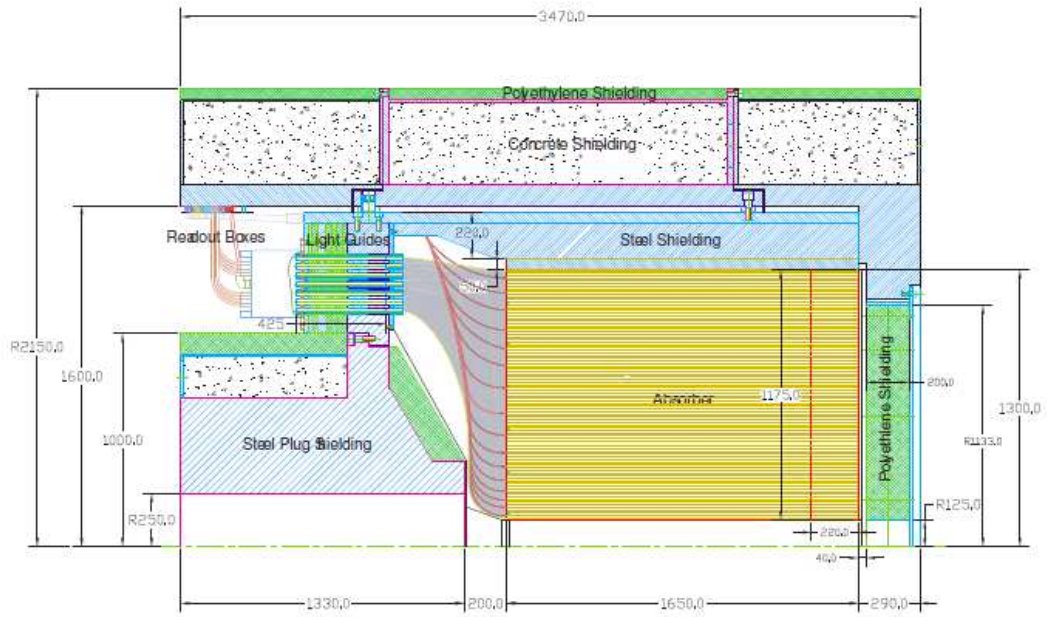
Figure 3.2.   The cross sectional view of HF

proton interaction is deposited into the two forward calorimeters, compared to only 100 GeV for the rest of the detector. In case of CMS at $|\eta| = 5$, HF will experience ~ 1 GRad at 5×10^5 pb^{-1} which correspond to ~ 10 years of LHC operation (Abdullin et al., 2008). Some results of a simulation are shown in Figure 3.3. (Akchurin et al., 2002). Figure 3.3.(a) shows the average calorimeter signal from 50 GeV γs versus time (i.e., integrated radiation dose), for photons entering the calorimeter at $\eta=4$ and $\eta=5$ and Figure 3.3.(b) shows the effects of the accumulated dose on the widths of these signal distributions. The horizontal axis is plotted on a scale linear in $N^{0.3}$, where N stands for the number of years of LHC operation.

Under such a hostile environment, one needs to use radiation hard optical active material. That's why fused-silica core with high hydroxyle content and polymer hard-clad fibers were chosen for CMS forward calorimeters. The monitoring of fibers transparency, damage due to irradiation and even more its recovery after irradiation is vital for calibration of the calorimeter. In this section radiation damage and recovery studies of regular HF quartz fibers using current HCAL readout chain of CMS are discussed.
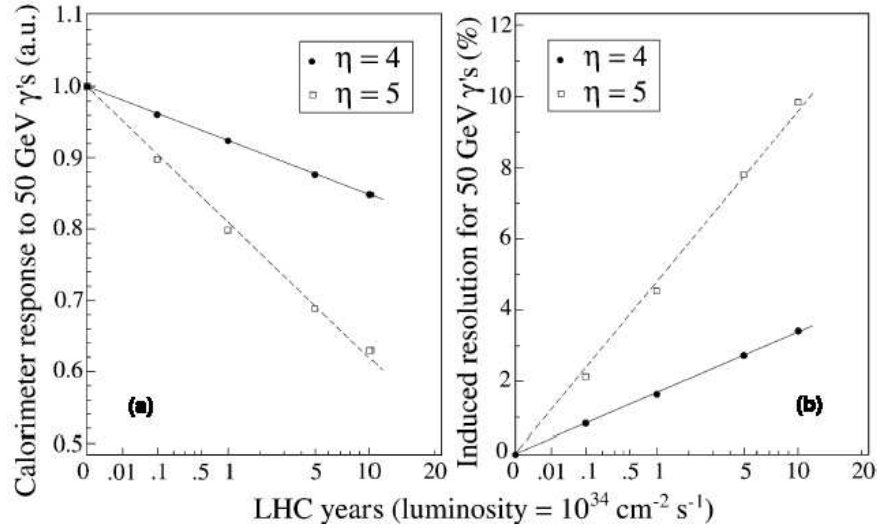
Figure 3.3.   The expected calorimeter response (a) and energy resolution (b) for 50 GeV γs entering the calorimeter at η 4 or 5, as a function of time during LHC operation at the nominal luminosity. The horizontal axis is plotted on a scale linear in $N^{0.3}$, where N stands for the time of LHC operation (Akchurin, 2003)

3.2   Radiation Monitoring with the RADDAM Device

HF is a quartz fiber calorimeter based on Čerenkov radiation detection of showers produced in iron by charged particles. The final products of the shower (mainly electrons) passing through the quartz fiber with a velocity greater than speed of light in the quartz generate Čerenkov light signal (threshold for electrons $E \geq 190$ keV). The fraction of the generated light is given by,

$$f_{trap} = \frac{NA}{2n_{core}^2} \tag{3.3}$$

where NA is the numerical aparture that is a dimensionless number that defines the range of angles at which the fiber can emit or accept light. In HF the fibers that are used have a fused-silica core 600±10 μm in diameter with 600^{+5}_{-10} μm hard-clad polymer and 800±30 m protective acrylate buffer. The fibers have $NA = 0.33\pm0.02$ and both ends are cleaved with a diamond cleaver[2]   (Baiatian, 2006). The optical attenuation in these

---

[2] Because of the losses, half of the light which hits the core-cladding intersection at larger than $71°$ which is the critical angle for HF multimode fiber can reach the PMT photocathode to produce a signal. The half-angle $\theta = 19^0$ is determined by the refractive indices of the core (n_{core}) and the cladding (n_{clad}), $\sin\theta = \sqrt{n_{core}^2 - n_{clad}^2}$

(a) HFM   (b) HFP
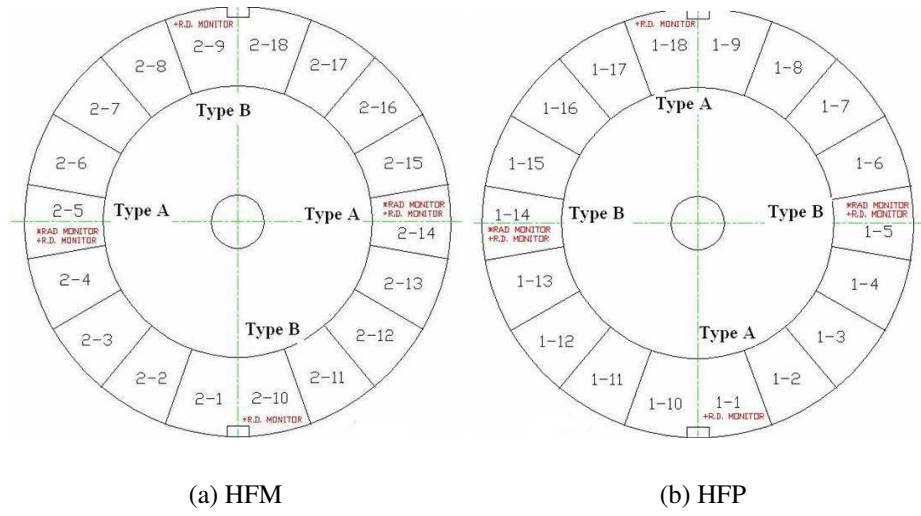
Figure 3.4.   7 towers of 8 wedges are equipped with Raddam fibers on HF in minus side (a), in plus side (b)

types of fibers scales as $a(\lambda)(D/D_0)^{b(\lambda)}$ where D is the accumulated dose, normalized to a reference dose (D_0 = 100 MRad) for convenience. For example, at 450 nm at the accumulated dose of D = 100 MRad, the induced attenuation is ∼1.5 dB/m, which simply equals a. The a and b parameters characterize the radiation hardness of a given fiber. For high OH⁻ (300-500 ppm) HF fibers at 450 nm, $a \approx$ 1.3 and $b \approx$ 0.3 (Dumanoglu et al., 2002; Akchurin et al., 2002; Thomas, 2004). As we will see later the recovery of the damage when one stops the data taking is critical in HF calibration.

3.2.1   Construction and operation of the RADDAM device

As discussed in the introduction of this chapter it is important to know the level of degradation in the active medium since healthy analysis depends on the calibration of the detector. In order to monitor the optical fiber transparency effected by the radiation and recovery of the fibers an optical monitoring device (RADDAM) has been developed which uses the light reflection at the two ends of 2.5 m long regular HF fiber. 56 RADDAM fibers have been installed in seven towers of four wedges in each of the two HF (See Figure 3.4.). The light of a pulsed nitrogen laser (337 nm) is shifted into the blue region, near 450 nm, where the Cerenkov light spectrum detected by the PMT's is maximum. The 7 towers cover the whole HF pseudorapidity range. The wave shifter is a 2 cm long blue scintillating fiber placed in a feed-through connector. The light sent to each RADDAM

23

fiber is read out by the regular tower PMT whose signal is registered through the QIE-HCAL-DAQ as in beam interaction data taking. But the dedicated RADDAM runs are taken out of particle beam to avoid mixing of laser light and Cerenkov light produced by showering particles. At LHC the RADDAM runs will be taken out of beam, in the orbit gap (between train of bunches) or in local runs when the LHC stops. The RADDAM
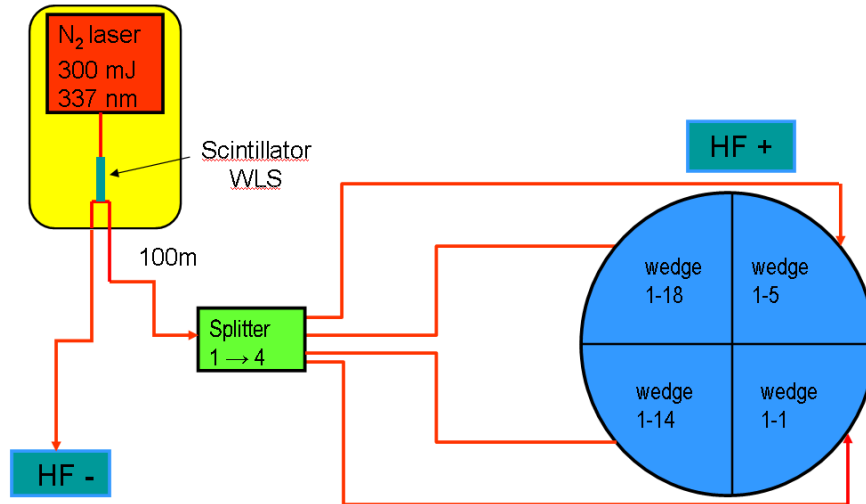
Figure 3.5.   Schematic drawing of the chain of the laser light distribution to the 56 RADDAM fibers

fibers, 2.5 m long are of the same type than the regular HF fiber, they have their two ends carefully polished to get the best reflection. One of the tower fiber is cut the part going to the PMT is kept in the tower bundle and the remaining part in the absorber is replaced by one RADDAM fiber. The laser light is distributed in the 7 RADDAM towers trough a splitter 1--→7 installed at the level of the Read out box of RADDAM wedges. As can be seen in Figure 3.6.(a) and (b) the RADDAM fiber is coupled with a small gap to the fiber which serves the incoming laser light and the fiber which carries the reflected light to the PMT, in a capillary. The chain of laser light distribution to the 56 RADDAM fibers is as follow, Laser → Splitter 1--→2 (HF's) → Splitter 1--→4 (HF wedges) → Splitter 1 --→ 7 (wedge towers) (see Figure 3.5.). By construction of the RADDAM device the regular data taking in LHC operation will not be disrupted even by a single fiber. The read out of the RADDAM device is identical to the HF read out in LHC operation.

The first reflection which is the reference signal is obtained in the capillary and the second from the end of the 2.5 m long fiber 25 ns later. Since the DAQ has a 25 ns width window
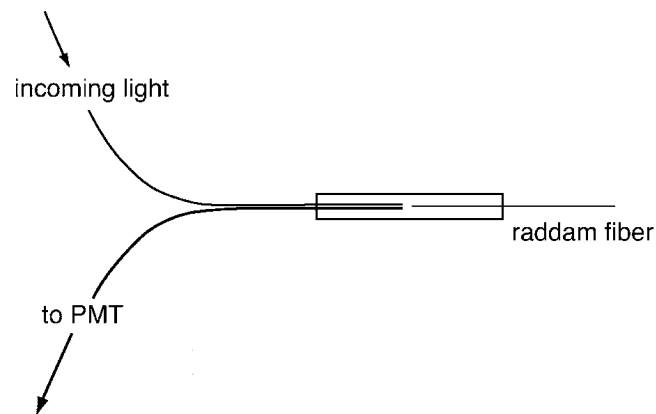
(a)
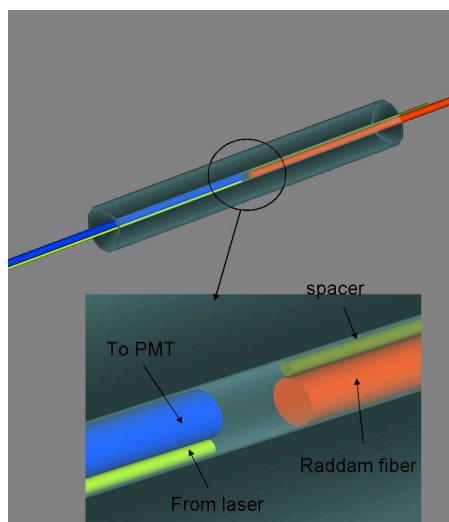
(b)

Figure 3.6.   The radiation damage to the optical transparency and its recover is monitored by a set of 56 fibers distributed in the entire calorimeter system. The ratio of the reflected pulse from the far end of the fiber located inside the absorber to the reflected pulse from the first optical connector provides a relative measure of fiber darkening. A schematic of optical connection is depicted in (a) and fiber coupling in capillary (b).

(TS), the first pulse and the second pulse are located in two consecutive TSs. The ratio of charge from the second to the first one is used as a measure of fiber darkening. The charge sharing in TSs is shown in Figure 3.7.
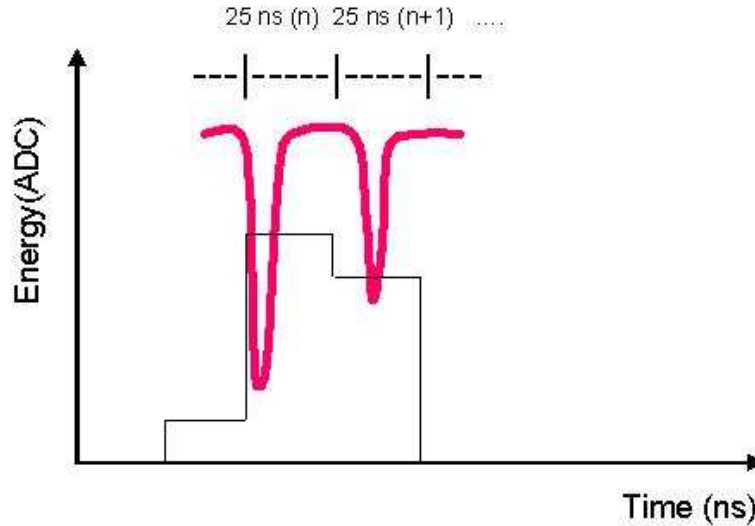
Figure 3.7.   Sharing of signals in time slices of RADDAM system

3.2.2   Previous studies

The darkening studies of different type of radiation hard quartz fibers were done by irradiation in a 500 MeV electrons beam of the Linac Injector of LEP (LIL) at CERN. Results were published in 2002 (Dumanoglu et.al., 2002). The transmission of Xe light was measured in situ in the 350-800 nm range and the induced attenuation at 450 nm was found to be 1.52±0.15 dB/m for a 100 Mrad absorbed dose (Dumanoglu, 2003). In 2004 Cankocak et. al. investigated the darkening of two high OH^- quartz fibres irradiated with 24 GeV protons at the CERN PS facility IRRAD (Glaser et. al., 1999). The tested fibres were 0.6mm quartz core diameter, one with hard plastic cladding (qp) used in HF and the other with quartz cladding (qq) for sake of comparison and thinking also to super LHC (SLHC) which is a proposed upgrade to the LHC to be made around 2012. The typical attenuation at 455nm for 100 Mrad dose was found to be 1.44±0.22 dB/m for qp and 2.20±0.15 dB/m for qq fiber (Cankocak, 2008). Two-parameter fits were used for darkening and recovery analysis in both of these studies. In the next sections the level of radiation damage and damage recovery is measured at IRRAD using the LHC HCAL

DAQ will be compared to the above parameters.

3.3   Beam test of RADDAM system in 2006

3.3.1   Experimental set-up

To measure directly the effect of irradiation on a RADDAM fiber we install one in a PS proton beam along the beam axis (T7 IRRAD PS beam). The fiber was attached to a support fixed on a remotely controlled table (see Figure 3.8.). In order to display and optimize the beam profile a luminescent screen with a camera was used (Glaser,1999).
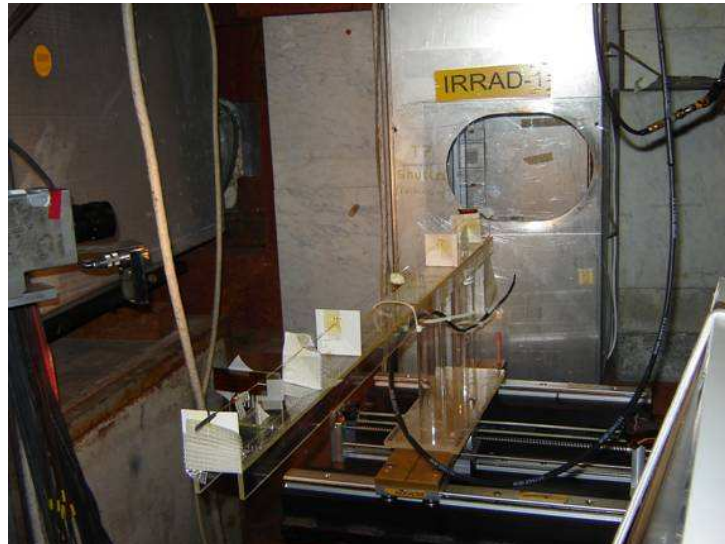
Figure 3.8.   Remotely controlled table at IRRAD

The sample fiber is 1% tilted relative to the beam to get 1m length (*L*) out of 2.5m swept in each cycle irradiated by proton flux of 10^{16}p/cm^2/h which corresponds to a 2.6 Mrad/h dose rate (see Figure 3.9.). The 24 GeV proton beam was delivered as 34 sub-cycles in a (19.6 ± 3.0) s long supercycle (Glaser,1999). This beam delivers 10^{11} protons/cm^2/burst in a spot of 2×2cm^2. The optical set-up uses a pulsed nitrogen laser (337nm) with 300 J of nominal output power a few nanoseconds duration with a frequency of 10.20 Hz but with a jitter time greater than $\pm$ 10 ns. The laser light was guided to the irradiated samples by a 36 m long 600 m diameter fused silica fiber. Another 36 m long fiber sent the transmitted light to the PMT installed in a shielded control room. The DAQ collected the data between the beam cycles to prevent the laser transmitted light
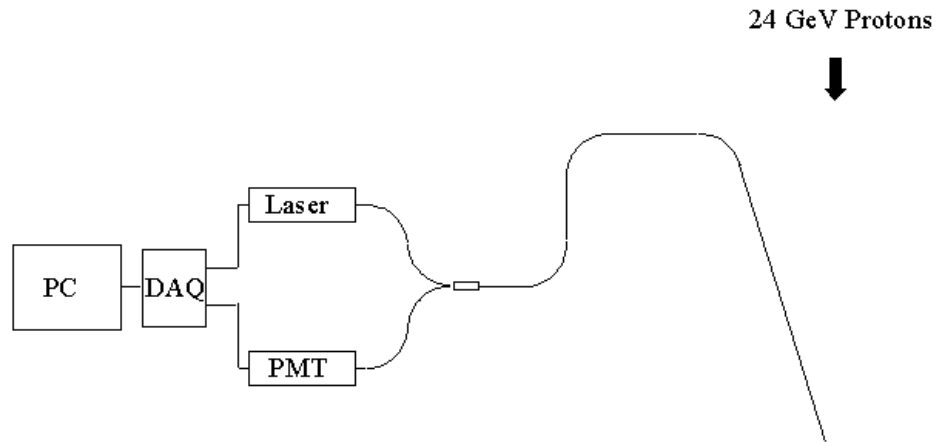
Figure 3.9.   RADDAM laser testbeam setup

from Čerenkov light produced by the proton beam.
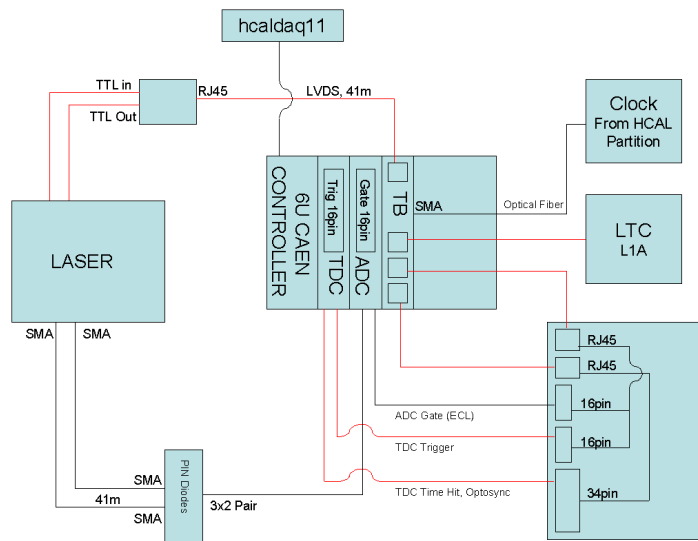
Figure 3.10.   RADDAM laser system setup

3.3.2   Data acquisition with the LHC-HCAL-DAQ

During the 2006 RADDAM device beam test we have used the Data Acquisition (DAQ) system of the LHC-HCAL data taking. The trigger signals were sent to the HCAL local DAQ to collect the data in correlation with the laser firing. The DAQ system, shown

in Figure 3.11., consisted of HCAL Trigger and Readout units (HTRs), TTC[3] system and HCAL Data Concentrator Card (DCC). The DAQ chain is described as follow: The laser light from the RADDAM fibers is transported to photo multiplier tube (PMT), with a standard bialkaline, 8-stage photomultiplier tube with a borosilicate glass window[4] , which converts the light into electrical charge. The charge signal is measured and encoded into a non-linear digital scale by the Charge Integrator (QIE). The QIE uses the LHC clock to divide time into regular bins and measures the accumulated charge in each time bin. Internally, the QIE uses capasitors to accumulate the charge and the voltage. There are four such capasitors in each QIE, and the QIE uses each capasitor in turn, discharging it for two clocks before using it again. This each subsequent time sample comes from different capasitor-id (CAPID). Each time bin is 25 ns long. The outputs of QIE channels are digitally combined onto a high-speed optical link and sent to HCAL Trigger/Readout board (HTR). The HTR board could accept eight fiber links, corresponding to twenty-four QIE channels. In our case one fiber was used. The HTR board buffers the incoming digital data and transfers it to the Data Concentrator Card (DCC) when a Level 1 Accept (L1A) is received. The DCC is responsible for collecting data from up to eighteen HTRs and transferring it on to the central DAQ. More information for DAQ system can be found at (Mans and Fisher, 2003).

3.3.3   Analysis and Results

3.3.3.1   Data taking

In order to avoid both beam contamination and Čerenkov light we used a logic unit as a trigger to tell DAQ when there is *no beam*. Since both damage and recovery in a qp fibre are very fast processes especially at the high dose rate used at IRRAD, we set up the DAQ to take events quite fast at the beginning of the irrradiation and slowly later. We trig the DAQ in a sequence file driven by a Run Control programme definining rate of runs

---

[3] The overall TTC system architecture provides for the distribution of synchronous timing, level-1 trigger, and broadcast and individually-addressed control signals, to electronics controllers with the appropriate phase relative to the LHC bunch structure, taking account of the different delays due to particle time-of-flight and signal propagation. Within each trigger distribution zone, the signals can be broadcast from a single laser source to several hundred destinations over a passive network composed of a hierarchy of optical tree couplers (http://ttc.web.cern.ch/TTC/)

[4] (R7525) Manufactured by Hamamatsu Photonics, Japan.
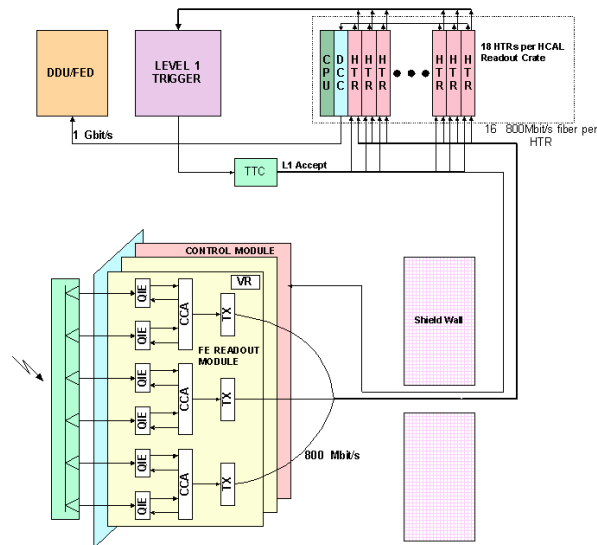
Figure 3.11.   HCAL Data Acquisition Setup

and number of events as follow,

- At the beginning, for 3 hours, every 3 minutes with 2 minutes ($\sim$400 elaser firings or events) data taking

- After 3 hours and for 3 hours every 10 minutes with 4 minutes ($\sim$800 events) data taking

- And then, every 1 hour with 4 minutes ($\sim$800 events) data taking.
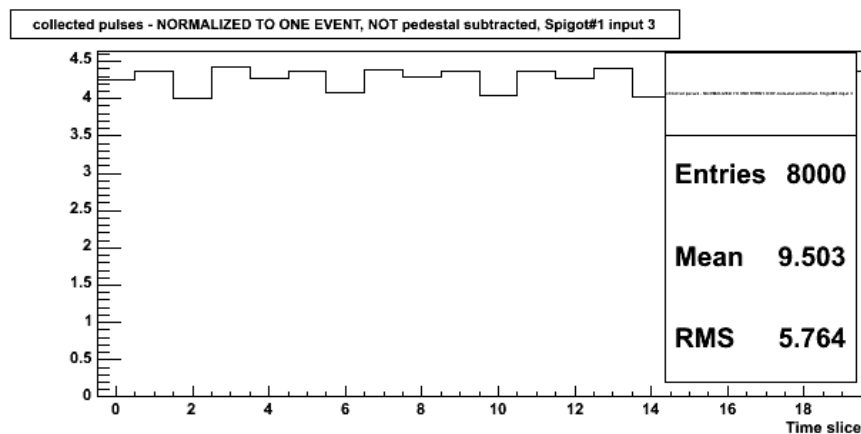
Figure 3.12.   Pedestal distributions over TSs

DAQ registered events in 20 TSs of 25 ns width. Pedestal was calculated as the mean of the first four TSs and subtracted from each TS (see   Figure 3.12.). The total charge in

linearized ADC is calculated by summing of 20 TSs after pedestal subtraction. The pulse height distribution can be seen in Figure 3.13.(a). Figure 3.13.(b) shows the timing of the signal. We have plotted charge sharing by TSs in order to see where the first and the second reflections occured. The pedestal subtracted pulse shape of RADDAM fiber signal in linearized ADC counts can be seen in Figure 3.14.(a). Since we don't know exactly the charge distributions in each TS because of the laser jitter, we obtained the ratio of the first reflection (S_1) over the second reflection (S_2), histogramming the ratios as a function of phase defined as TTC-Laser trigger in Figure 3.14.(b). This histogramme of the ratio $R = S1/S2$ versus phase is used to the fit the ratio in the "plateau" range of phase where the ratio values are stable. The plateau corresponds to events where S1 and S2 are well centered in consecutive time slices. In fact 90% of one PMT signal is contained in one 25ns time slice (CMS Collaboration, 1997b).

The ratio R fitted values to plateaux of phase histogramme for over 500 runs, are plotted as a function of time of irradiation in Figure 3.15.(a). There are two beams on and two beams off stages which are used for radiation damage and damage recovery analysis. We calculated the ratios $I(\lambda,D)/I(\lambda,0)$ which decrease as a of function time which correspond to the dose absorbed as shown in Figure 3.15.(b). The light attenuation $A(\lambda,D)$ in the qp fibre is given by the following formula according to Dumanoglu(2002) and Griscom(1993):

$$A(\lambda,D) = \alpha(\lambda)[D/D_s]^{\beta(\lambda)} \tag{3.4}$$

α and β parameters were calculated by Cankocak et. al. (2008) and Dumanoglu et. al.(2002)(see Table 3.1.) by fitting the ratios as a function of wavelength and dose by,

$$I(\lambda,D)/I(\lambda,0) = \exp[-(L/4.343)\alpha(\lambda)(D/D_s)^{\beta(\lambda)}] \tag{3.5}$$

where the scale factor $D_s = 100$ Mrad, L is the length of the fiber irradiated, in metres and α is the attenuation at 100 Mrad in dB/m. Substituting the Eq. 3.4 in Eq. 3.5 we get the ratio as a function of attenuation by,
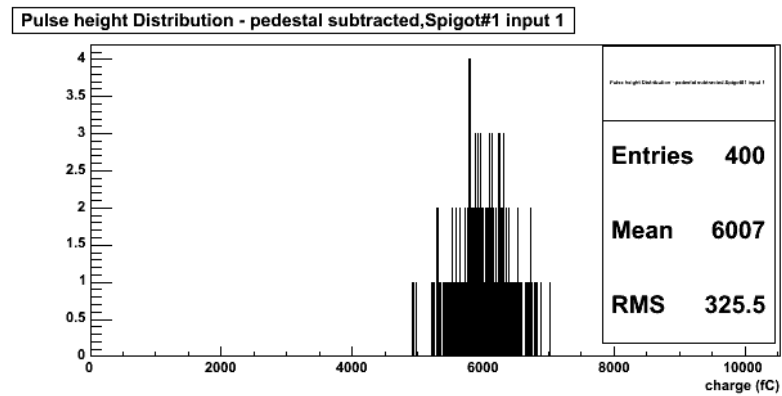
(a)
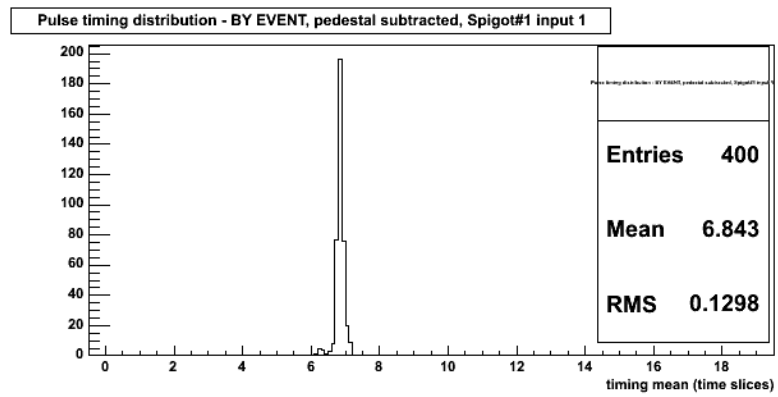
(b)

Figure 3.13.   Linearized pulse height distribution(a), Timing of pulses(b)
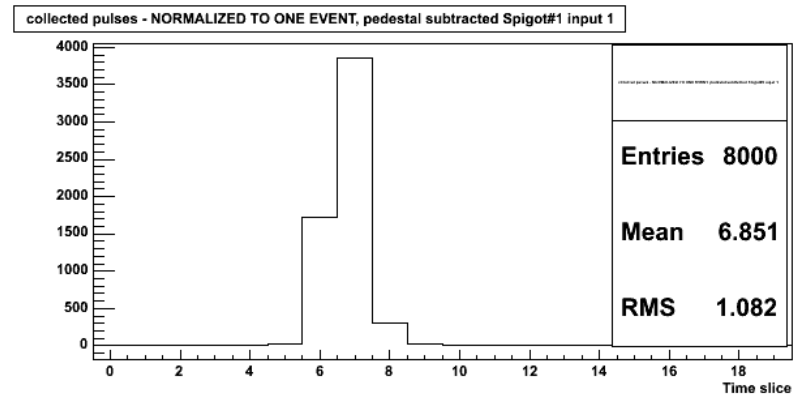
(a)
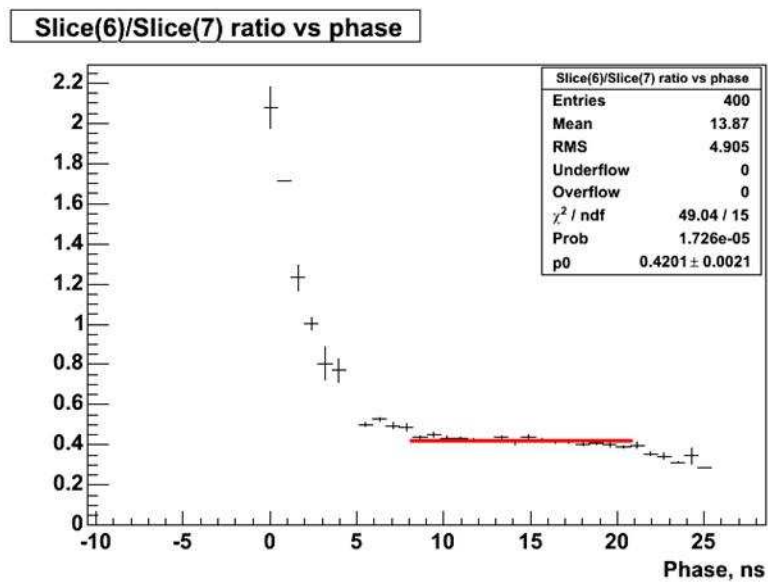
(b)

Figure 3.14.   Sharing of charge by TSs. It can be seen that first reflection is in 6th TS and second in 7th TS (a), S_1/S_2 versus phase(b)

33
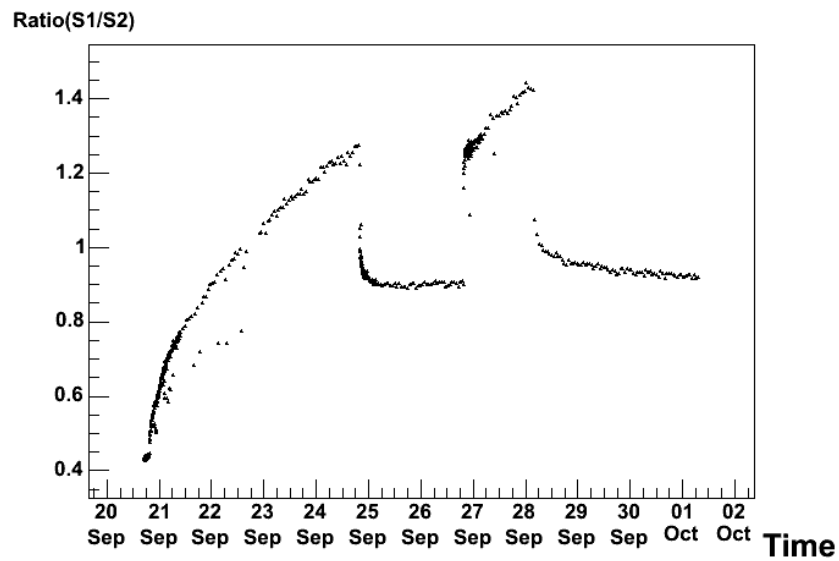
(a)
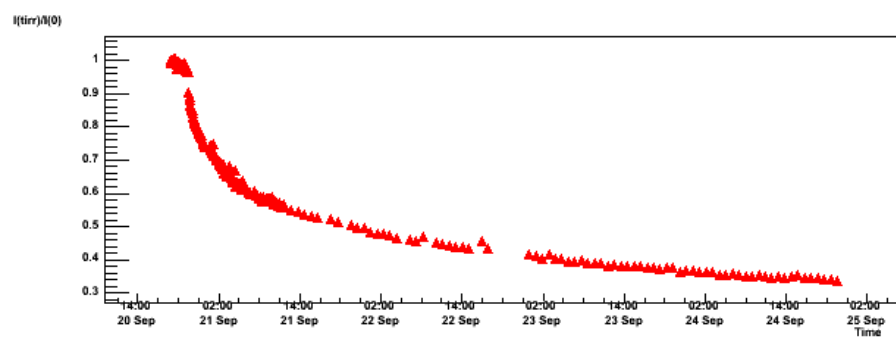
(b)

Figure 3.15.   Overall ratios calculated as S_1/S_2 versus time (a), $I(\lambda,D)/I(\lambda,0)$ versus time(b)

$$I(\lambda,D)/I(\lambda,0) = \exp[-A(\lambda,D)L/4.343] \tag{3.6}$$

Table 3.1.   Values of α, β parameters at 455 and 615 nm for qq and qp fibres of 0.6 and 0.3 mm quartz core diameter irradiated with protons (Cankocak et al., 2008) and electrons (Dumanoglu et.al., 2002)

Fibre	α(455-460nm)	β(455-460nm)
qq(0.6)p	2.20±0.06	0.53±0.013
qp(0.6)p	1.44±0.16	0.44±0.05
qp(0.3)e$^-$	1.54±0.02	0.33±0.001

In the present tests we calculated the attenuation A from the ratio of reflected signals at the end of the first period of irradiation at time t_{irr} about 25 September Figure 3.15.(b):

$$R(D) = \frac{S_1}{S_2(D)} \tag{3.7}$$

where S_1 is independent of dose D. So the ratio is calculated as,

$$\frac{I(\lambda,D)}{I(\lambda,0)} = \frac{R(0)}{R(D)} = \frac{S_2(D)}{S_2(0)} = 0.33 \tag{3.8}$$

Since the light crosses twice the fiber length, $L = 2$ m,,

$$A(\lambda,D) = -\left(\frac{4.343}{2}\right)\log\left[\frac{I(\lambda,D)}{I(\lambda,0)}\right] = 2.40\text{dB/m} \tag{3.9}$$

From the measured parameters of Cankocak et al (2008) we estimated the dose to be 250 Mrad from the formula:

$$D = D_s\left[\frac{A(\lambda,D)}{\alpha(450)}\right]^{1/\beta} = 250\text{Mrad} \tag{3.10}$$

where D_s = 100 Mrad, $\alpha(450)$ = 1.60 dB/m and $\beta(450)$ = 0.44 from Cankocak et. al.(2008).

3.3.3.2   Damage recovery analysis and results

The HF iron-quartz fiber-PMT has a maximum of sensitivity at 450 nm and at this wavelength that the recovery effect is maximum (Cankocak et. al., 2008; Merlo, 2007) The change in the attenuation with time is given as function of λ, t and t_{irr},

$$A_D(\lambda,t) = \frac{A(\lambda,D)}{(1+[\gamma(\lambda)(\frac{t}{t_{irr}})^{\eta(\lambda)}])} \qquad (3.11)$$

where $A_D(\lambda,t)$ is the value of the light attenuation at the post exposure time t (in hour) after an irradiation at a dose D in a time t_{irr} (Cankocak et.al.,2008; Dumanoglu et al., 2002; Griscom et. al.,1993). The increase of the transmitted signal $I_d(t)$ after an irradiation to a total dose D in time t_{irr} can be derived from Eqs. 3.4, 3.5 and 3.11 as,

$$I_d(t)/I(D) = exp[A(D)(\frac{L}{4.343})(\frac{\gamma t^{\eta}}{t_{irr}^{\eta}+\gamma t^{\eta}})] \qquad (3.12)$$

At 450nm the value of the parameter (450) is maximum and close to 1. The radiation damage recovery in 24 hours was measured in qp fibres after a dose accumulation of 310 Mrad(127 hours irradiation). The huge effect of recovery can be seen from Figure 3.16., one day after the stop of irradiation the reflected signal increases by about ~50%. Using the Eq. 3.12 we calculated the ratio of $I_d(t)/I(D)$=1.58 with $\gamma = 1$, $\eta = 0.30$, $t/t_{irr} = 0.189$ and $A = 2.614$ dB/m.
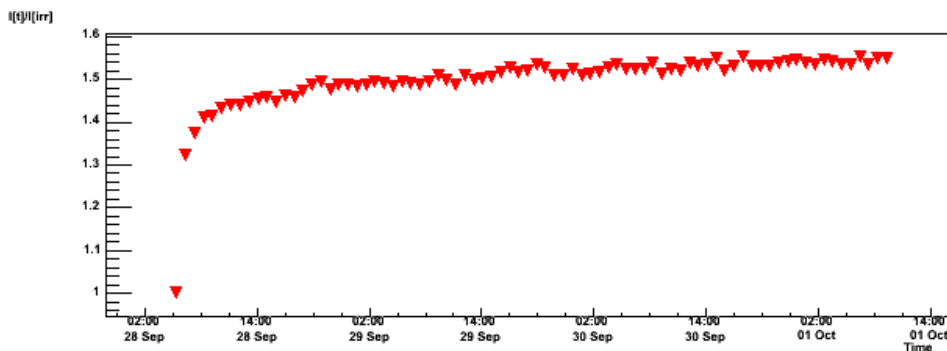
Figure 3.16.   Recovery of the damage giving an increase of the transmitted signal versus the post irradiation time for qp fibre at 455nm after 310 Mrad irradiation

The knowledge of the recovery effect is essential to know the status of the HF fibers at

the time of data taking when a source calibration is made few days or few weeks after the end of data taking. Otherwise the calibration will give the image of a too good detector not corresponding to the reality of the detector during data taking.

4. CASTOR PROTOTYPE-II PERFORMANCE STUDIES

4.1 Introduction

As one of the very forward calorimeters of the CMS experiment, the **C**entauro And **ST**range **O**bject **R**esearch (CASTOR) detector will survey heavy ion and proton - proton (*pp*) collisions at LHC. It is a quartz - tungsten sampling calorimeter that will be installed 14.38 m from the interaction point (IP) and will cover $5.15 < \eta < 6.6$. It's pseudo rapidity coverage contributes to the hermeticity of CMS, thus, allowing missing transverse energy (MET) to be measured more precisely which is very important for beyond standard model physics so called new physics. Since jet reconstruction is a vital process for finding Higgs production channel the vector-boson-fusion described by concomitant radiation of two jets forward/backward rapidities, CASTOR will give us reconstruction/tagging information in η range beyond HFs. Furthermore, in order to make precise background subtracted measurements, we have to understand the soft interactions between the remnants of the colliding protons which leads to offset in energy and the multiplicity in the underlying event. CASTOR together with TOTEM will provide information on forward particle production and will help to the tuning of Monte Carlo Generators. So in addition to it's heavy ion programme CASTOR will also contribute to diffractive and low-*x* physics in pp collisions (CASTOR Engineering Design Report (EDR), 2007).

4.2 Technical description
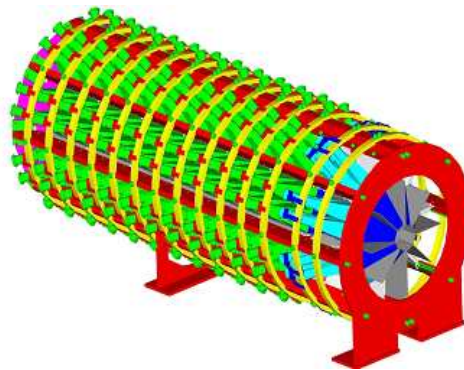
Figure 4.1.   Schematic design drawing of the full CASTOR calorimeter.

As a calorimeter the CASTOR dedector is based on Čerenkov-effect. It consists of tungsten (W) plates as absorber interleaved by fused silica quartz (Q) plates as active media. When the charged particles pass through the quartz medium the Čerenkov light is produced and then collected and focused by aircore light guides that couple to PMT's where the Čerenkov light is converted into a signal. The sides of the Q plates were covered with Tyvek paper in order to protect them from damage by the W plates and also to reflect back the escaping light from Q plates. The calorimeter is divided into 16 divisions radially around the beam pipe and segmented into 14 sections longitudinally (see Figure 4.1.). Each tungsten (W)-quartz (Q) pair is called sampling unit (SU) and each redout unit (RU) is consists of 5 SUs. From the IP, the first 2 RUs are called the electromagnetic (EM) part. The W/Q plates of thickness 5 mm and 2 mm are used in the EM part. The remaining 12 RUs are called the hadronic (HAD) part and the W/Q plates of thickness 10 mm and 4 mm are used in this part. Thus, one calorimeter has 16x14=224 channels in total (see Figure 4.2.).

In order to yield maximum Čerenkov light output the layers are inclined at 45° from the beam direction to allow charged particles to have a longer mean free path. The index of refraction of quartz is n = 1.46-1.55 for wavelengths $\lambda = 600 - 200$ nm. The corresponding Cherenkov threshold velocity is $c = 1/n$ = 0.65-0.69, and therefore, for β_c 1 the angle of emission is $\theta_c = \arccos(1/n\beta) = 46°$- 50°(CASTOR EDR, 2007)

4.2.1   Tungsten plates

As mentioned before W plates are used in CASTOR calorimeter as absorber. The W plates made of tungsten alloy, fabricated by Stark GmbH, are composed of 97% W, 1.3 % Fe and 1.7% Ni and have density 18.5±0.2 g/cm^3. The thickness of W plates for EM/HAD part is 5 mm/10 mm but the effective thickness is 7.07 mm/14.14 mm at 45° respectively. The shape and dimensions of W plates can be seen in Figure 4.3.

4.2.2   Quartz plates

Semi-octant geometry is chosen for Q plates and they are positioned side by side along their vertical sides separated optically by a thin Al foil. Thus, the calorimeter has
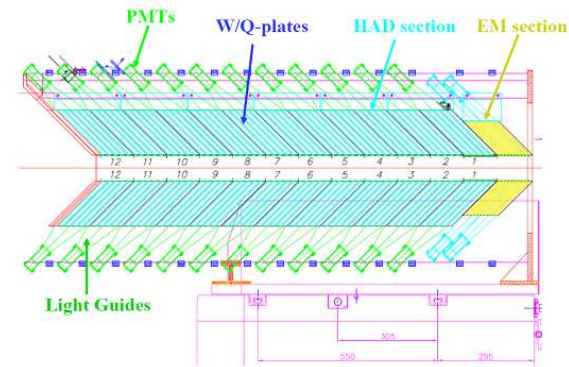
(a)
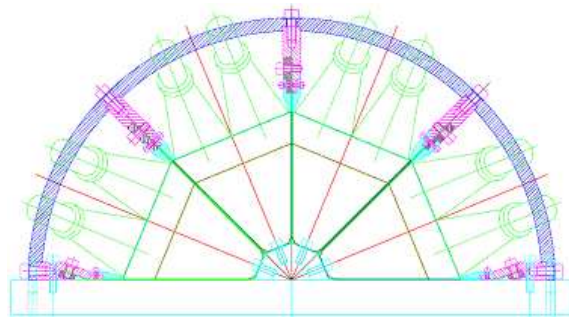
(b)

Figure 4.2.   Longitudinal crossectional view of of CASTOR calorimeter design(a) and Front view of of the CASTOR calorimeter design (b) (CASTOR EDR, 2007).
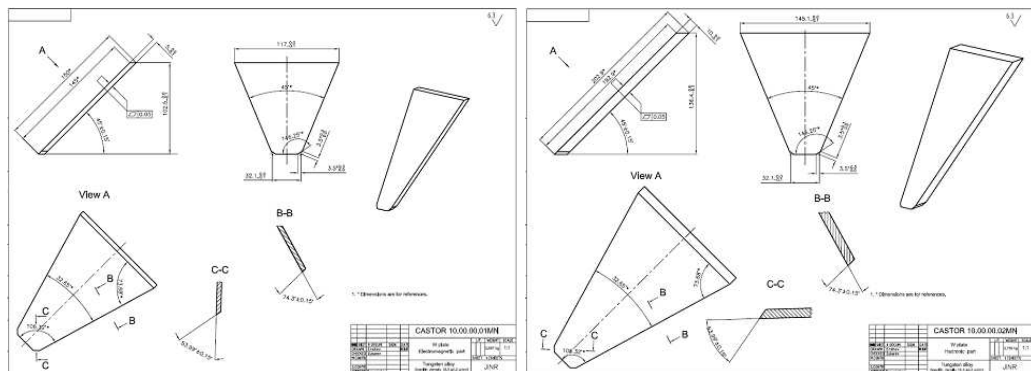
(a)   (b)

Figure 4.3.   The octant trapezoidal shape and dimensions of EM W plate(a) The octant trapezoidal shape and dimensions of EM W plate(b) (CASTOR EDR, 2007).

16 azimuthal segments. The thickness of Q plates for EM/HAD part is 2 mm/5 mm but the effective thickness is 2.80 mm/5.60 mm at 45° respectively. The shape and dimensions of

Q plates can be seen in Figure 4.4.

(a)   (b)

Figure 4.4.   The octant trapezoidal shape and dimensions of EM Q plate(a) The octant trapezoidal shape and dimensions of HAD Q plate(b) (CASTOR EDR, 2007).

4.2.3   Light guides

(a)   (b)

Figure 4.5.   Cross section of the EM light-guide with the PMT and base housing(a) Cross section of the HAD light-guide with the PMT and base housing(b) (CASTOR EDR, 2007).

The Čerenkov light produced in quartz plates is guided through to the readout unit (APD, PMT) from the upper edge of quartz plates by an aircore light guide. Because the performance of the calorimeter depends on the light transmission efficiency the design and positioning of the light guides is a very crucial subject. A GEANT 3.21 based

code is developed to simulate the transmission of Čerenkov photons through a light guide (Aslanoglou et al., 2007). Figure 4.5. shows the shapes and dimensions of EM and HAD light guides.

4.3   Beam tests of CASTOR prototype II

According to beam test and simulation results of CASTOR prototype - I (Aslanoglou et al., 2007a) we constructed and tested the CASTOR prototype - II using tungsten and quartz plates, avalanche photo diodes(APDs) and PMTs for readout and air-core light guides which has reflective foil inside (Dupont polyester film reflector coated with AlO and reflection enhancing dielectric layer stack SiO_2+TiO_2) for light transmission. The second prototype has a semi-octant ($\phi = 22.5$) shape. The CASTOR prototype - II calorimeter is made up of two sections which are electromagnetic (EM) and hadronic (HAD) (see Figure 4.6.). They are both built up of tungsten plates as absorber and fused silica quartz plates as active medium. There are 4 semi-octant shape EM sections which have independent readout units and 4 octant shape HAD sections. The Čerenkov light produced in quartz plates by relativistic particles are collected and focused by air-core light guides onto the APDs or PMTs.
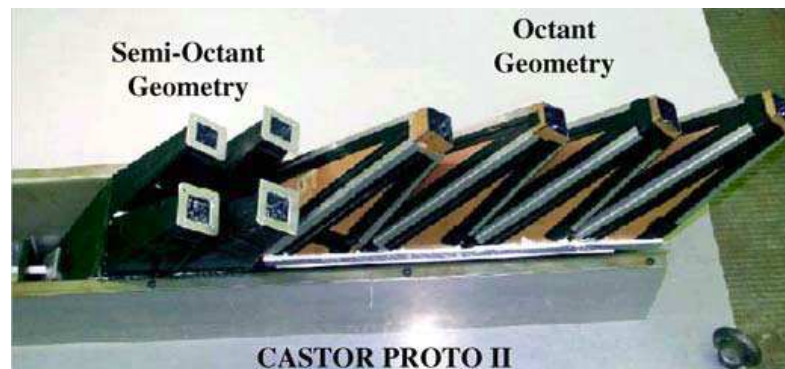
Figure 4.6.   Picture of the CASTOR prototype II calorimeter before assembling the photodetectors. The semi-octant geometry of the EM section (length: 14 cm) and the octant geometry of the HAD section (length: 40 cm) can be seen (Aslanoglou et al., 2007b).

4.3.1   Tungsten - quartz plates and photodetectors

The specifications of the tungsten that is used for construction of the calorimeter as absorber are $\lambda_I = 10.0$ cm, $X_0 = 0.365$ cm and density = 18.5 g/cm^3. In the electromagnetic section the thickness of W/Q plates are 3 mm/1.5 mm respectively. The thickness of W/Q plates in the HAD section are a little bit larger than the EM section, 5 mm/2 mm respectively. The successive W/Q layers are inclined 45° w.r.t the incoming beam direction in order to boost Čerenkov light output. Tyvek paper is used to cover large sides of Q plates to protect them from W plates and reflect back the escaping light. The top edge of W plates are polished and the others are painted with reflecting paint. Each sampling unit (SU) corresponds to $1.218X_0$, or $4.88 \times 10^2\lambda_I$ in EM section and each readout unit (RU) consists of 11 SUs and is $13.4X_0$, or $0.536\lambda_I$ deep. The EM section has a total length of $26.8X_0$ or $1.072\lambda_I$. A sampling unit in HAD section corresponds to $7.96 \times 10^2\lambda_I$ and each readout unit consists of 10 SUs and is $0.796\lambda_I$ deep. The HAD section has 4 RUs, corresponding to $3.186\lambda_I$. In total, the whole prototype has $4.26\lambda_I$ in total (see Figure 4.7.)(Aslanoglou, 2007b).
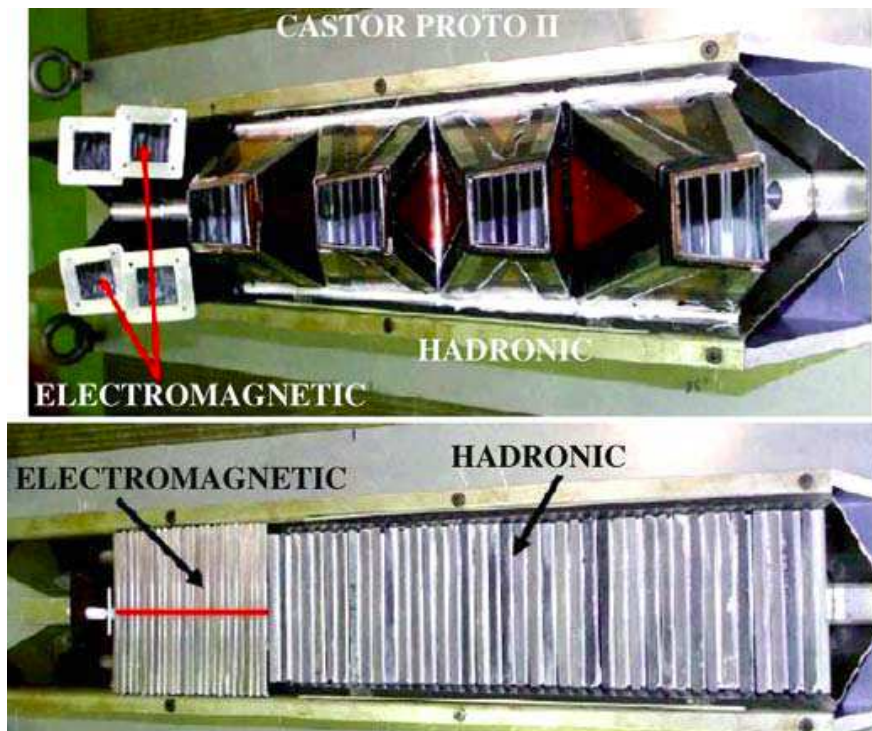
Figure 4.7.   Upper photograph of the W/Q-plates of the CASTOR prototype-II showing the EM and HAD sections (lower picture) and the light guides (upper picture) in the semi-octant (octant) geometry of the EM (HAD) sections respectively (Aslanoglou et al., 2007b).

The Čerenkov photons are detected by photodetector devices which were used in prototype II are a matrix of 2x2 or 2x3 Hamamatsu S8148 APDs. The 2x2 matrix APDs have 1 cm^2 total area and the 2x3 matrix APDs have 1.5 cm^2 total area. They are coupled to air-core light guides that are covered with Dupond [AlO+SiO2+TiO2] reflective foil inside(Figure 4.8.).
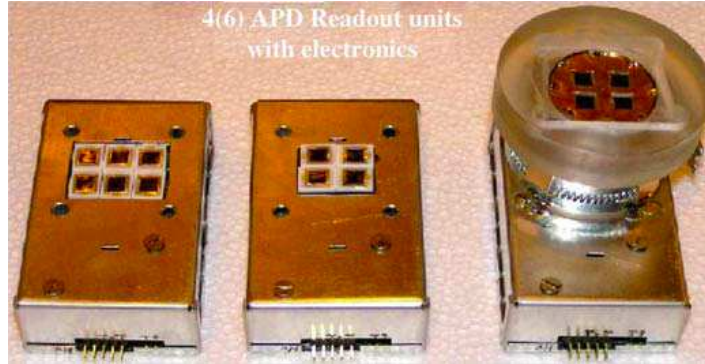
Figure 4.8.   Assembled APD readout units with 4 and 6 APDs (Aslanoglou et al., 2007b).

4.3.2   Analysis and results

The CASTOR prototype - II was tested at H2 beam line of Super Proton Synchrotron (SPS) at CERN in 2004. The SPS provides 400 GeV/c protons which are converted into different type of particles in a Berillium target (T2) such as electrons, pions (π^-) and muons (μ^-), then these particles are sent to H2 beam line. The momentum of the produced particles has a range from 10 to 350 GeV/c. The tracking information of particles was given by 7 wire chambers (WC) which are WC1 through WC3 and WCA, WCB, WCC and WCD providing $\sim 350\mu$m spatial resolution in both x- and y- coordinates. In order to get beam trigger three scintillation counters S1, S2 and S4 were used in coincidence with the area of 2×2 cm^2, 4×4 cm^2 and 14×14 cm^2 respectively. For muon tagging muon veto counters also were used (Figure 4.9.).

The assembled CASTOR prototype - II which was used in the beam test 2004 can be seen in Figure 4.10. It was placed on a movable table w.r.t incoming beam particle direction in x- and y- directions. The electromagnetic and hadronic sections were scanned with 20 - 200GeV electrons, 20 - 350GeV pions and 50,150 GeV muons in order to get energy responses. Thanks to WCs and SCs we were able to know where the particles hit
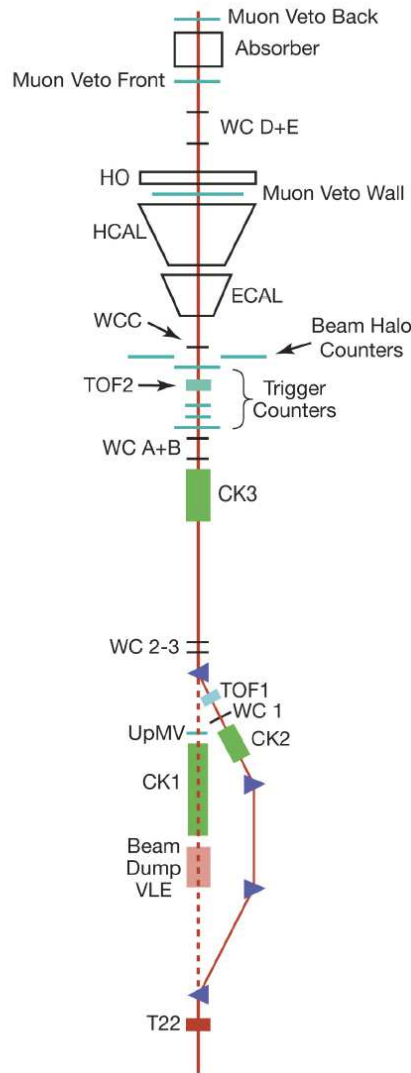
Figure 4.9.   The CERN H2 beam line and the experimental setup are shown schematically.

the prototype and this information was used for the spatial resolution calculations.

For spatial resolution the calorimeter was scanned vertically and horizontally with both electron and pion beams. Figure 4.11. shows projection of the CASTOR prototype II onto a plane at 45° w.r.t to the beam axis. Dashed red lines and blue lines correspond to hadronic and electromagnetic sections of the calorimeter respectively. The numbers represent the points used for the vertical and horizontal scans. *x-y* coordinates of these points can be seen in Table 4.1. In order to have more impact points the beam profile of each point was subdivided into a number of smaller parts.
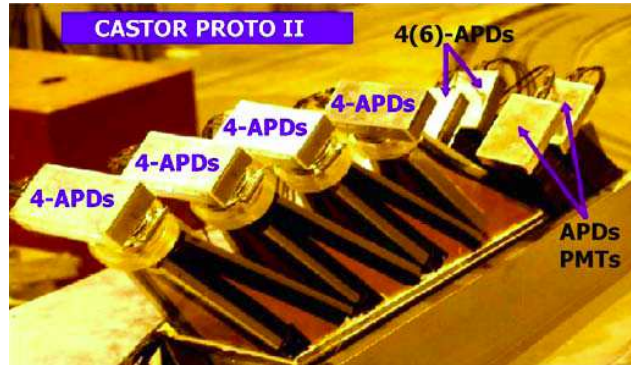
Figure 4.10.   Assembled prototype II on the moving table in the CERN/SPS H2 beam line. Only the APD readout units are shown (Aslanoglou et al., 2007b).
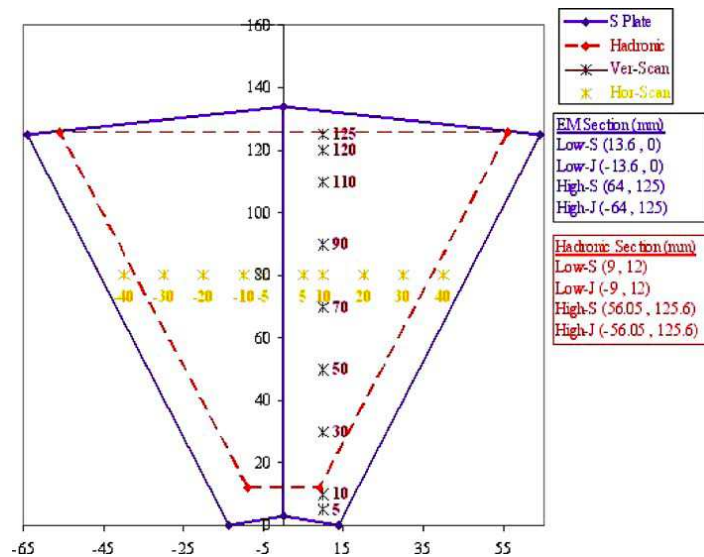
Figure 4.11.   Projection of the EM (blue) and HAD (red) sections onto a 45° plane. The numbers indicate the *x-y* coordinates of the beam impact points used in the horizontal and vertical scans (Aslanoglou et al., 2007b).

Table 4.1.   The (*x*, *y*) coordinates (mm) of the impact points of the horizontal and vertical scans for both electron and hadron beams

		Electron Scan			
Vertical scan	*x*	*y*	Horizontal scan	*x*	*y*
A	10	5	A/	-40	80
B	10	10	B/	-30	80
C	10	30	C/	-20	80
D	10	50	D/	-10	80
E	10	70	E/	-5	80
F	10	90	F/	5	80
G	10	110	G/	10	80
H	10	120	H/	20	80
I	10	125	I/	30	80
			J/	40	80

4.3.2.1   Energy response

For position resolution of the EM section of the prototype, electron beams of energy 100 GeV were used. Figure 4.12. shows the spectrum measured with 20 and 200 GeV electrons hitting on the EM section of the prototype equipped with 2×2 and 4×4 APDs. The energy response of the calorimeter is found to be Gaussian for all energies.

4.3.2.2   Spatial resolution

Position scans not only give us information on the transverse distribution of the electron showers but also it gives chance to check uniformity of the calorimeter. Using WC information we applied a beam cut and Figure 4.13. shows the electron beam profile hitting the left semi-octant of the prototype after the cut. Scanning the horizontal hit positions according to the coordinates listed in Table 4.1., EM shower width and response behavior close to the edge were estimated.

The results of the horizontal-scan analysis with 100 GeV electrons are shown in Figure 4.14. for the 4 APDs readout configuration. Figure 4.14.- left shows the response of the two adjacent (leftright) EM semi-octants as the beam impact point moves across the front face of the calorimeter. The sigmoid nature of each response curve is evident. In Figure 4.14.-right, the *x*-derivative of the response is calculated, giving the width of the electromagnetic shower. We observe that one standard deviation amounts to 1.7 mm.
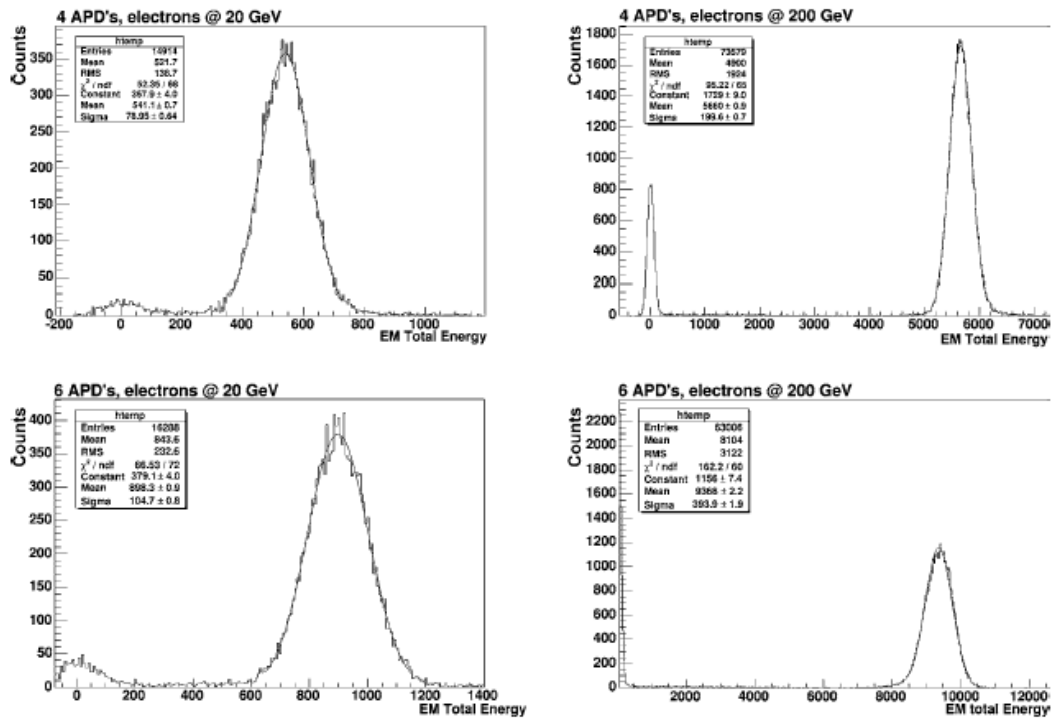
Figure 4.12.   Energy response of the EM calorimeter to electron beams of 20 and 200 GeV obtained with 4 APDs (upper plots) and 6 APDs (bottom plots) (Aslanoglou et al., 2007b).
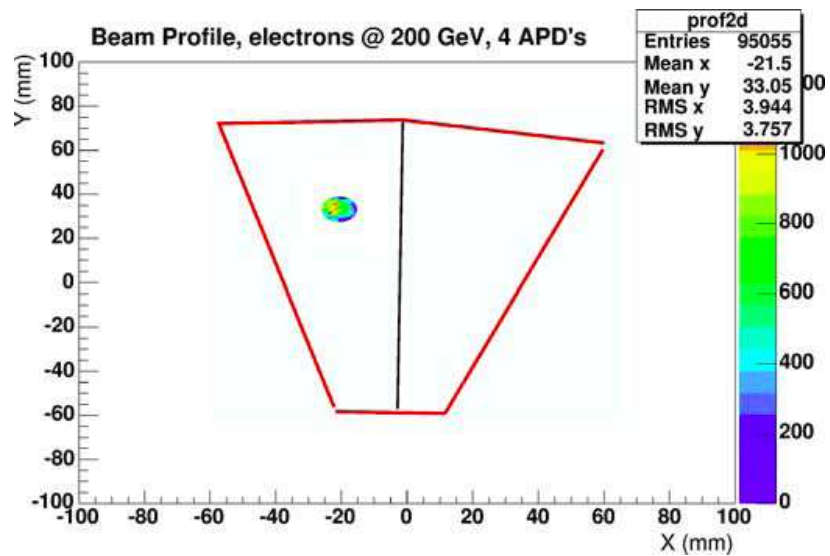
Figure 4.13.   Profile of 200 GeV electron impinging on the left semioctant of the calorimeter, as measured by the scintillator-wirechamber telescope upstream of the prototype (Aslanoglou et al., 2007b).
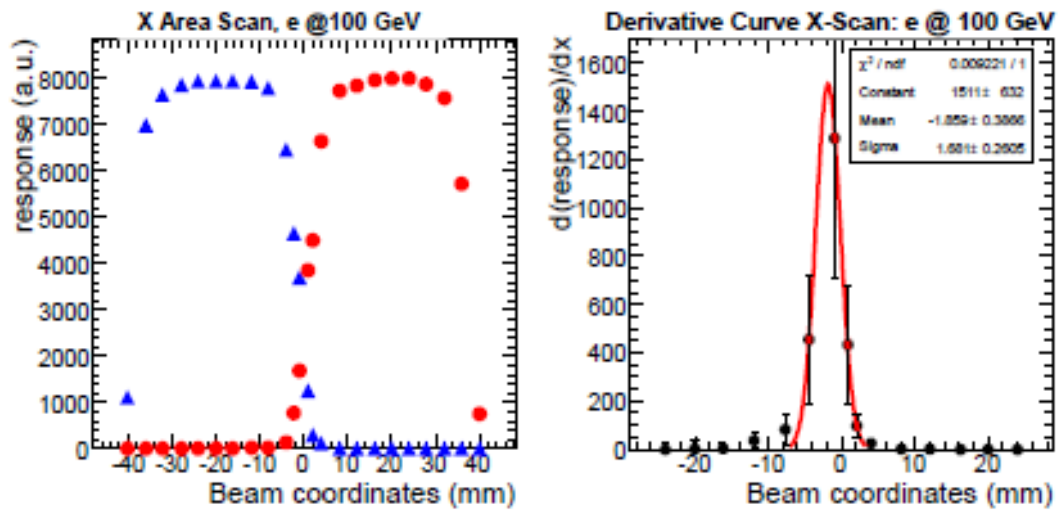
Figure 4.14.   Left: Response of the left and right semi-octant sectors of the EM section as the beam scans the front face of the calorimeter. Right : The derivative of the response with respect to *x*, indicating the width of the EM shower (Aslanoglou et al., 2007b).

5. CALIBRATION OF HCAL WITH COSMIC MUONS

5.1   Introduction

Until the first pp collisions from the LHC, the most powerful source of data for CMS is cosmic-ray events. We can calibrate and test HCAL components with cosmic-ray muons, thus improving our understanding of the detector (Bakirci et al., 2007). Both the HE and HB have been instrumented with readout boxes containing Hybrid-PhotoDiodes (HPDs) and Charge, Integrate and Encode readout (QIE) chips. The functionality of the on-detector electronics has been validated using the LED calibration system and using Co^{60} radioactive sources. The primary purpose of the SATOCRICH project (**S**pecial **A**ssignment to **O**bserve **C**osmic **R**ays **in CMS H**CAL) was to collect and analyze the first sample of cosmic-ray events for calibration of CMS HCAL. Another aim of the project was the preparations for the Magnet Test/Cosmic Challenge (MTCC) which was done in fall 2006. Figure 5.1. shows the eight HB+ wedges and muon barrels (MB) which were readout during MTCC.

5.2   Experimental Setup

5.2.1   Description of the setup

Three set of scintillator counters called V1, V2 and V4 were used to generate cosmic-ray event triggers. The counter V4, 35 cm x 110 cm, 5 cm thick, was mounted on the outer radius of the half-barrel, on top of the outer side of wedge 6 (TOP wedge). It was placed along the *eta-* axis of TOP wedge, covering approximately $\eta$ towers 1-4 and two central 5 degree ϕ slices. Counters V1 and V2, each 40 cm x 80 cm, 5 cm thick, were placed inside the half-barrel, on the inner side of wedge 15 (BOTTOM wedge). A photograph of the HB+ half-barrel, with trigger counters and readout cables is shown on Figure 5.2.. Each 20 degree wedge of HCAL Barrel is segmented into four 5 degree sectors. For historical reasons, we refer to the two external-in-ϕ sectors as Side (S) sectors and two internal-in-ϕ sectors as Middle (M) sectors. In η, each HCAL half-barrel is segmented into 16 towers, each covering $\Delta\eta = 0.08$. Longitudinally, each tower is sampled by up
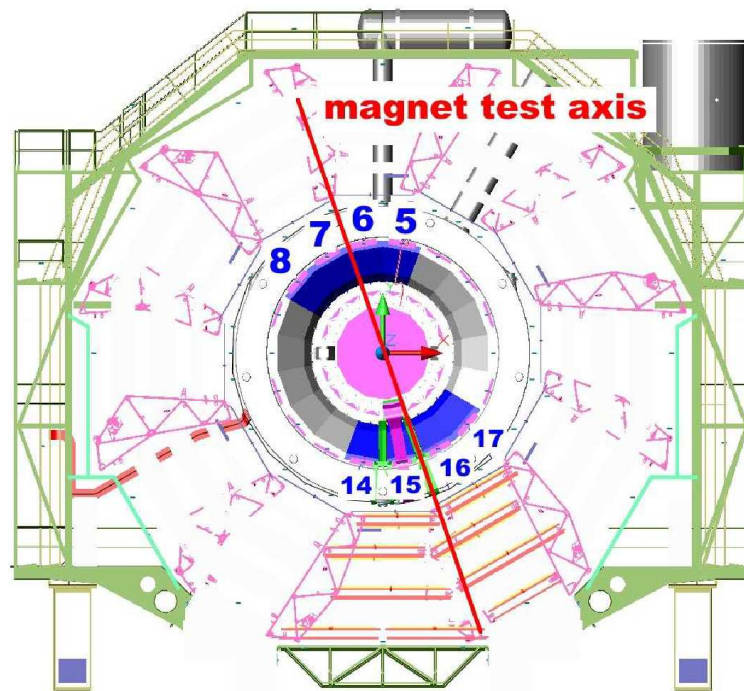
Figure 5.1.   View of CMS detector with eight HB+ wedges (5-8 and 14-17) read out during magnet test/cosmic challenge. Shown in yellow, are also two MB sectors (10 and 11), which were read out during MTCC. For SATOCRICH project, only two 20 degree wedges were read out: wedge 6 on the top and wedge 15 on the bottom. The drawing was prepared by David Simek (FSU/CMS Integration Office).

Figure 5.2.   A photograph of the HB+ half-barrel, with trigger counters and two wedges connected to readout cables. This picture was taken September 8, 2005. In the low η region one can see the trigger counters used for this exercise. Wedges 5 (at the top of the half-barrel) and 15 (at the bottom of the half-barrel) were used to collect cosmic dataset (Bakirci M.N. et al., 2007).

to 17 layers which are L00 through L16. L00 is the inner most layer whereas L16 is external most layer. Figure 5.3. shows scintillator layers and η segmentation for HB wedge. Additional information about CMS HCAL can be found in (CMS Collaboration, 1997b).
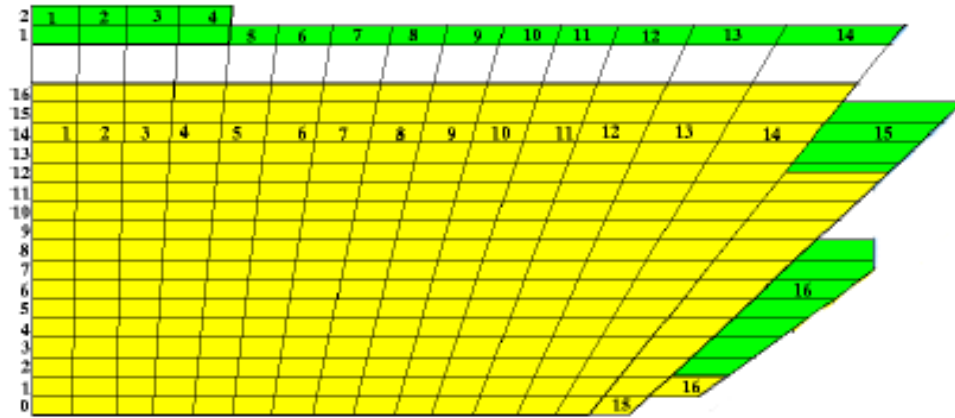
Figure 5.3. Scintillator layers and η segmentation for HB wedge. Longitudinally, $\eta - \phi$ towers are sampled by up to 17 layers. Note that some layers do not extend to the high η region, towers 14, 15 and 16.

Two different configurations have been used for data taking with the trigger counters V1 and V2. In *Configuration A*, counters V1 and V2 were oriented along the η axis covering approximately η towers 1-4 and two central 5 degree ϕ slices of wedge 15 (BOTTOM wedge). *In Configuration B*, counters V1 and V2 were oriented perpendicularly to the η axis covering approximately η towers 1-2 and provided full coverage in ϕ for BOTTOM wedge. Schematic drawings of two of these configurations are shown on Figure 5.4. and Figure 5.5.. The trigger was obtained such a way that analog signals coming from the scintillation counters were discriminated and then a three-fold coincidence was required as shown on Figure 5.6.(a). The high voltage settings for the counters V1, V2 and V4 were 2150 V, 2400 V and 2000 V respectively during HCAL 2004 TestBeam. The singles rates were order of 1 kHz for each trigger counter with 30 mV discriminator thresholds. The trigger rate for configuration A and configuration B were approximately 1800 triggers/h and 1300 triggers/h (20 triggers per minute) respectively. The accidental coincidence rate was negligible (less than 1 percent), verified by delaying one of the counters by 100 ns and measuring the coincidence rate. The coincidence trigger signals which were obtained from the counters were sent to the HCAL local DAQ to collect the
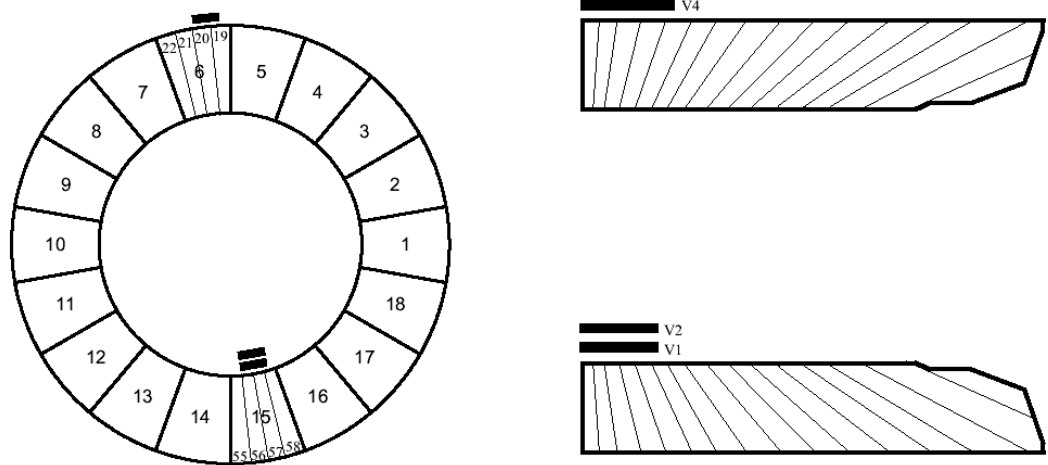
(a) HB+ view from interaction pint (IP)

(b) HB+ side view
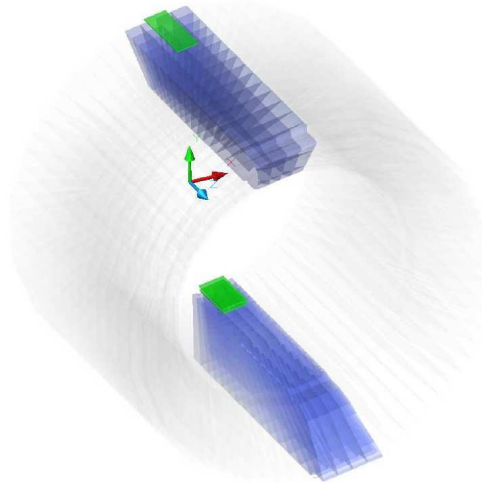
(c) HB+ 3D view

Figure 5.4.   The layout of counters for Configuration A (Bakirci M.N. et al., 2007)

(a) HB+ view from interaction pint (IP)

(b) HB+ side view

(c) HB+ 3D view
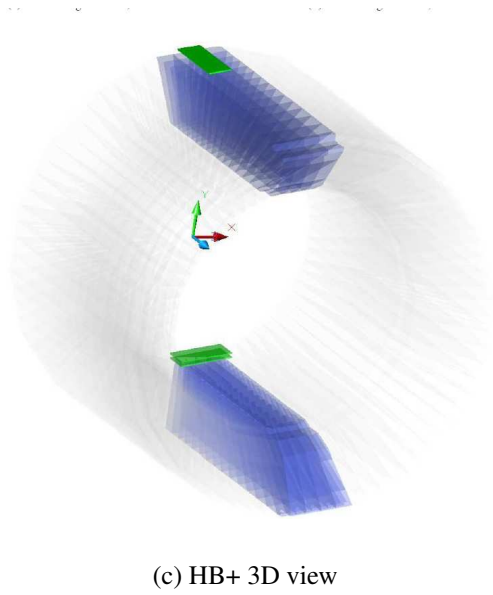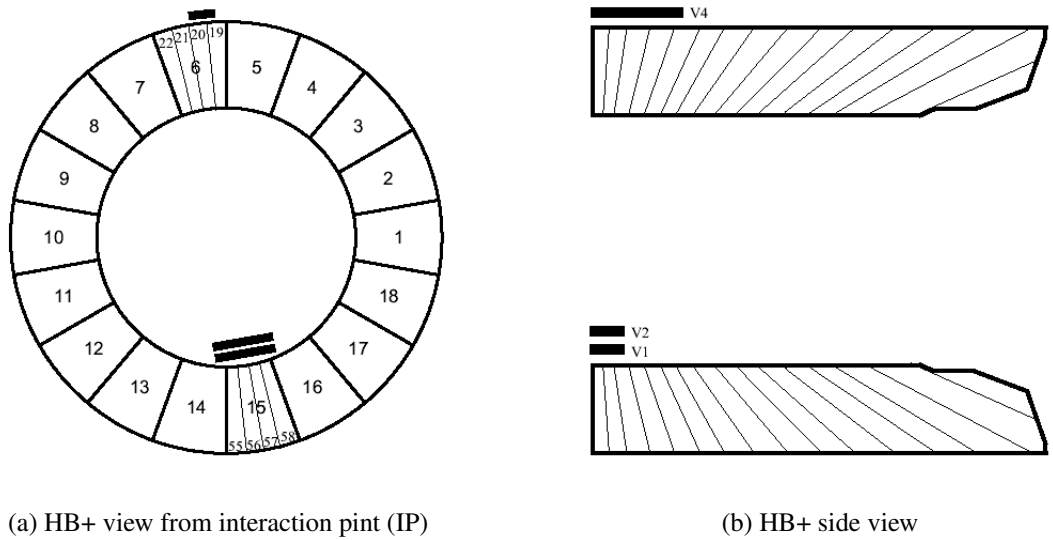
Figure 5.5.   The layout of counters for configuration B (Bakirci M.N. et al., 2007)

data. The trigger and DAQ system used for SATOCRICH is shown in Figure 5.6.(b). The DAQ system consisted of four HCAL Trigger and Readout units (HTRs), one TTC system and one HCAL Data Concentrator Card (DCC). The HTR cards receive the data from HB front-ends continuously over optical links and transmit the data to the DCC over TTC system when Level-1 Accept was received. The HCAL DCC can support up to fifteen inputs (spigots). We have used only eight of them in such a way that Spigots 1- 4 were used for the readout of wedge 6 (TOP), corresponding to ϕ sectors 19-22 and Spigots 11-14 were used for the readout of wedge 15 (BOTTOM), corresponding to ϕ sectors 55-58 in CMS naming convention. Analog light signals from HCAL scintillator tiles in each ϕ sector were converted to electronic pulses by Hybrid- PhotoDiodes (HPDs), with photocathode subdivided into 19 individual pixels. Electronic signals from HPDs were digitized by QIE (Charge, Integrate and Encode) chips.

5.2.2   Analysis and results

5.2.2.1   Data samples

We have recorded a background run triggering the DAQ using only the counter V1 discriminator, running approximately at a 1 kHz rate, in order to understand energy and timing distributions. Using the V1.V2.V4 coincidence two cosmic-ray (signal) runs were recorded. Table 5.1. shows the set of runs for the the analysis described in this chapter.

Table 5.1.   The set of runs used during SATOCRICH (Bakirci M.N. et al., 2007)

Run type	Run number	Events (N)
First SATOCRICH run	829	10
Pedestal run (only Bottom wedge)	928	1000
Background run (V1 trigger only)	956	20000
Signal run (V1.V2.V4 trigger) , conf A	957	80000
Signal run (V1.V2.V4 trigger) , conf B	990	50000
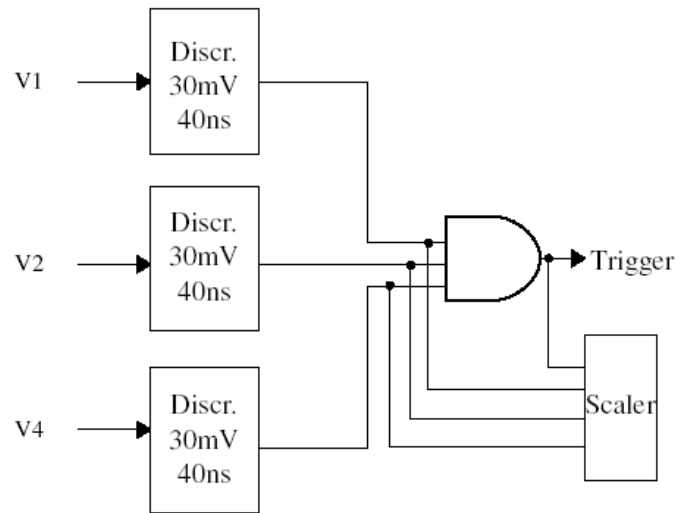
(a)
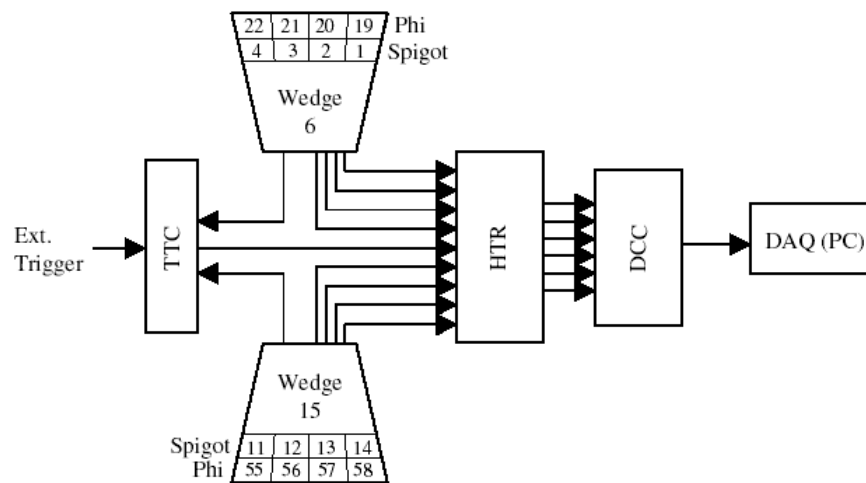
(b)

Figure 5.6.   Diagram of the SATOCRICH trigger system (a), Diagram of the SATOCRICH DAQ system (b) (Bakirci M.N. et al., 2007)

5.2.2.2   Pedestal definition

The event-by-event method was used to calculate pedestals. For each event, first four time slices (0-3) were defined as the pedestal region. Similarly the signal region was defined using time slices 8-11. In order to study pedestal stability and optimize pedestal definition, the pedestal run was analyzed for 1k events. Figure 5.7. shows the energy distributions for QIE sums for the region 0-3 time slices for the pedestal run r829, HTR channel 6.
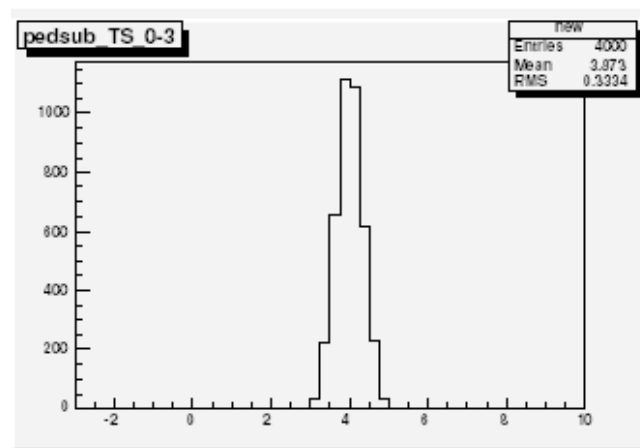
Figure 5.7.   Energy distributions for the region 0-3 for the pedestal run r829, HTR channel 6 (Bakirci M.N. et al., 2007)

5.2.2.3   Timing of muon signal

Figure 5.7.shows the energy weighted timing distribution of the first ten cosmic-ray events recorded from the data from very first SATOCRICH run with two wedges read out with 200 mV discriminator threshold settings. It can be seen from the Figure 5.8., the timing of events in the upper plot (TOP wedge) is approximately 9.5 time slices and the mean timing of events in the lower plot (BOTTOM wedge) is approximately 10.0 time slices. Taking into account that 1 time slice = 25 ns width, the time difference between TOP and BOTTOM wedges is approximately 12 ns which is consistent with the expected time-of-flight of muons across the distance between the two wedges (4.5 m) assuming the speed 30 cm/ns. That means the system were indeed triggering on the cosmic-ray events.
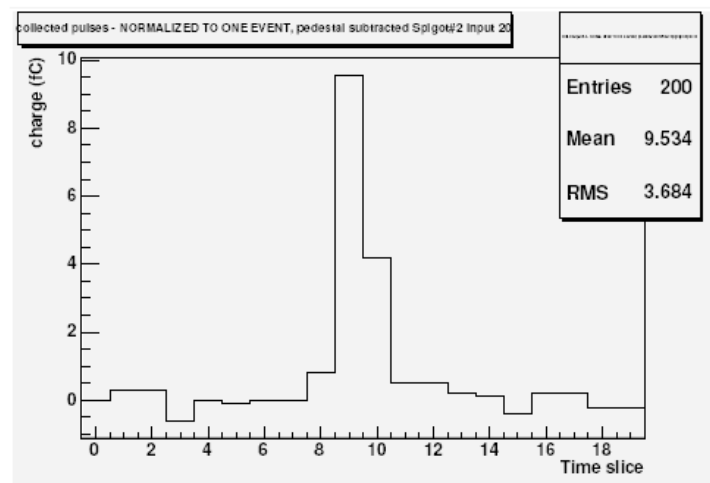
(a)
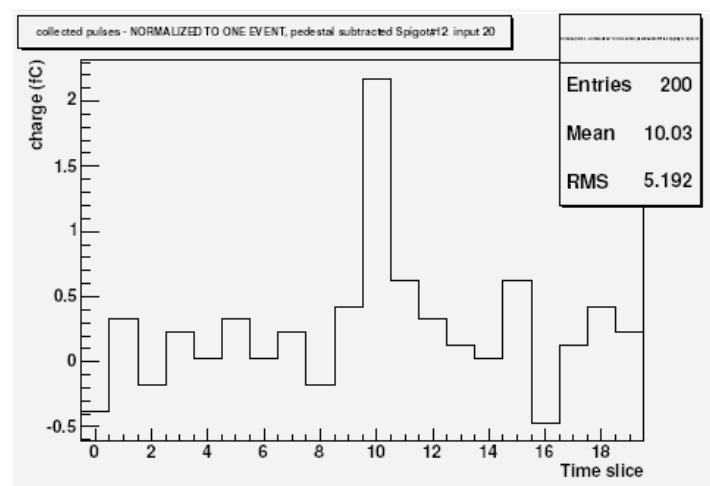
(b)

Figure 5.8.   Timing of the TOP wedge (a), Timing of the BOTTOM wedge (b) (Bakirci M.N. et al., 2007)

5.2.2.4 Event selection

In this section, the selection of cosmic-ray events is described. After pedestal subtraction the energy deposited in each $\eta - \phi$ tower was defined. Then, the seed tower candidate (the tower with highest energy) in TOP and BOTTOM wedges were searched. The requirement for the seed tower was the pedestal subtracted energy in the range 5 fC$< E_{seed} <$50 fC. Finally fiducial cuts were applied to make sure that the η of the seed tower is consistent with the coverage of the trigger counters. This cut should keep cosmic-ray single muon events but eliminate cosmic-ray showers. Such events would have more than one particle hitting HCAL, one of the particles passing through trigger counter, the other going through η towers not covered by trigger counters.

5.2.2.5 Energy calculation

The energy was calculated in fC using the ADC to fC conversion table. Table 5.2. shows the result of conversion of qie channel to fC using dcc→convert2fC(qie) function. The qie channels vary from 0 to 127 (7 bit ADC).

5.2.2.6 Events passing cuts

The number of events which passed according to corresponding configurations can be seen at Table 5.3.

Figure 5.9. shows the energy distributions of seed tower candidates for signal and background runs. As can be seen from the figure, almost all seed tower candidates for background run (V1 trigger only) have energy below 5 fC. However, for the signal run (V1.V2.V4 trigger), energy spectrum for seed tower candidates peaks at 3 fC and extends to 20 fC. There are also some events with seed tower energy above 50 fC. Based on these plots we chose to require 5 fC$< E_{seed} <$50 fC.

Figure 5.10. shows η distributions for seed tower candidates for signal runs in configuration A and configuration B, as well as for the background run. For signal runs, these distributions are consistent with the coverage of the trigger counters. Approximately 10%

Table 5.2.: Conversion table of qie channel to fC

	0	1	2	3	4	5	6	7	8	9
qie	0	1	2	3	4	5	6	7	8	9
convert2fC(qie)	-0.50	0.50	1.50	2.50	3.50	4.50	5.50	6.50	7.50	8.50
qie	10	11	12	13	14	15	16	17	18	19
convert2fC(qie)	9.5	10.5	11.5	12.5	13.5	15.	17.	19.	21.	23.
qie	20	21	22	23	24	25	26	27	28	29
convert2fC(qie)	25.	27.	29.5	32.5	35.5	38.5	42.	46.	50.	54.5
qie	30	31	32	33	34	35	36	37	38	39
convert2fC(qie)	59.5	64.5	59.5	64.5	69.5	74.5	79.5	84.5	89.5	94.50
qie	40	41	42	43	44	45	46	47	48	49
convert2fC(qie)	99.5	104.5	109.5	114.5	119.5	124.5	129.5	137.	147.	157.
qie	50	51	52	53	54	55	56	57	58	59
convert2fC(qie)	167.	177.	187.	197.	209.5	224.5	239.5	254.5	272.	292.
qie	60	61	62	63	64	65	66	67	68	69
convert2fC(qie)	312.	334.5	359.5	384.5	359.5	384.5	409.5	434.5	459.5	484.
qie	70	71	72	73	74	75	76	77	78	79
convert2fC(qie)	509.5	534.5	559.5	584.5	609.5	634.5	659.5	684.5	709.5	747.
qie	80	81	82	83	84	85	86	87	88	89
convert2fC(qie)	797.	847.	897.	947.	997.	1047.	1109.5	1184.5	1259.5	1334.5
qie	90	91	92	93	94	95	96	97	98	99
convert2fC(qie)	1422.	1522.	1622.	1734.5	1859.5	1984.5	1859.5	1984.5	2109.5	2234.
qie	100	101	102	103	104	105	106	107	108	109
convert2fC(qie)	359.5	2484.5	2609.5	2734.5	2859.5	2984.5	3109.5	3234.5	3359.5	3484.5
qie	110	111	112	113	114	115	116	117	118	119
convert2fC(qie)	3609.5	3797.	4047.	4297.	4547.	4797.	5047.	5297.	5609.5	5984.5
qie	120	121	122	123	124	125	126	127		
convert2fC(qie)	6359.5	6734.5	7172.	7672.	8172.	8734.5	9359.5	9984.5		

Table 5.3.   Number of events passing cosmic-ray muon selection cuts (Bakirci M.N. et al., 2007)
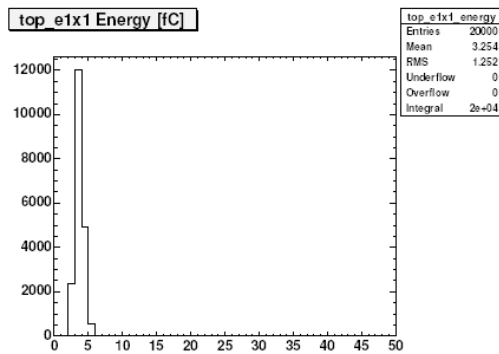
configuration	Background	config A	config B
Run	Run 956	Run 957	Run 990
Total	20,000	80,000	50,000
Passed 5 fC$< E_{TOP} <$50 fC	145	27,685	18,496
5 fC$< E_{TOP} <$50 fC and 5 fC$< E_{BOTTOM} <$50 fC	2	8621	5100
Passed Fiducial Requirement	0	7357	4384
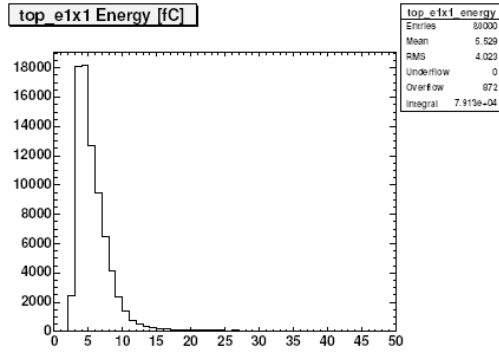
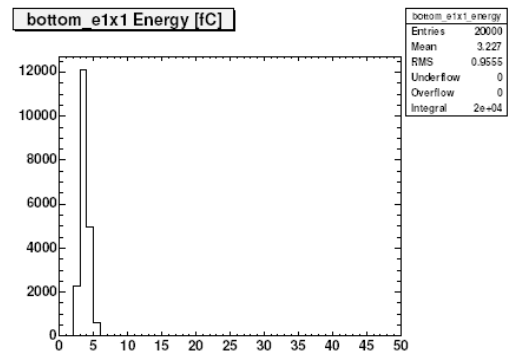(a) Signal Run. TOP: energy of seed tower candidate
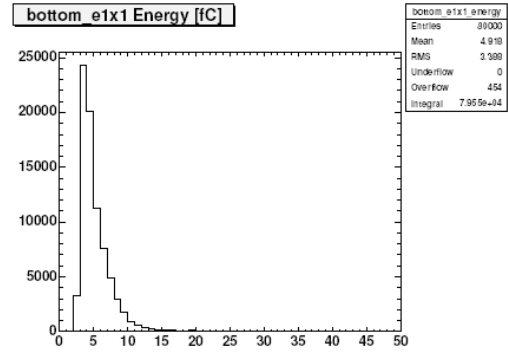
(b) Signal Run. BOTTOM: energy of seed tower candidate

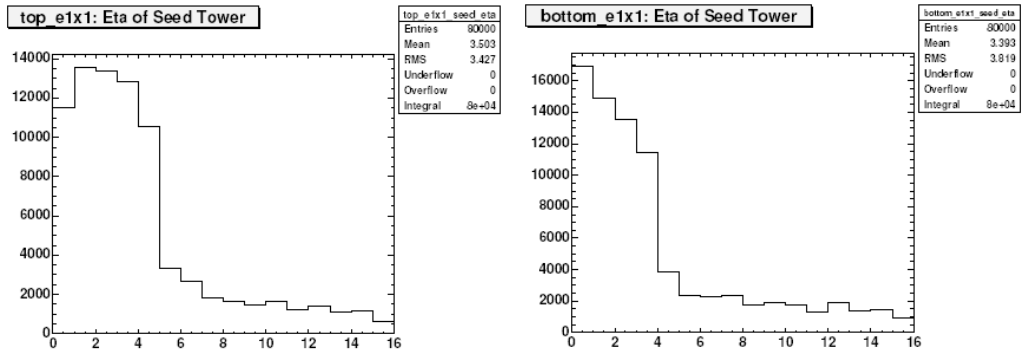(c) Background Run. TOP: energy of seed tower candidate

(d) Background Run. BOTTOM: energy of seed tower candidate

Figure 5.9.   Energy distributions of seed tower candidates for signal run: (a) TOP and (b) BOTTOM; for background run: (c) TOP and (d) BOTTOM (Bakirci M.N. et al., 2007)

of events have seed towers outside of the fiducial volume of the trigger counters. These are very likely multi-particle cosmic shower events, when one of the particles hits the trigger counters, and the other, more energetic goes through other part of the wedge. In order to remove such events from our sample, we apply a fiducial volume cut, $\eta_{top} < 5$. For the background run, the number of events decreases as a function of η tower number. This is simply an artifact of search algorithm, which starts looping from $\eta = 1$. Figure 5.11. shows ϕ distributions for seed tower candidates for signal runs in configuration A and B, as well as for the background run. The figure shows that distributions are flat for the background run and are consistent with the layout of the trigger counters for the cosmic ray runs.

We have compared energy distributions for e1x1 (energy deposited in the seed tower), e3x3 (energy deposited in a 3x3 tower cluster around the seed tower) and e5x5 (energy deposited in a 5x5 tower cluster around the seed tower) energy clusters for TOP and BOT-TOM wedges for signal run for configuration A. In the event selection, we require that e1x1 energy cluster are 5 fC$< E_{seed} <$50 fC. This cut is visible in the e1x1 distributions, shown in the top raw plots. Figure 5.12. shows scatter plots of energy distributions of the TOP cluster vs energy of the BOTTOM cluster for the events passing 5 fC cuts. Figure 5.13. shows average cosmic-ray muon energy vs size of cluster (e1x1, e3x3, e5x5). The mean energy of e3x3 clusters is significantly higher than that of e1x1 clusters. Note that in the testbeam, muons traverse only a single tower. Therefore muon energy is fully contained by e1x1 energy cluster. However, cosmic-ray muons cross multiple towers of HCAL. Therefore only e3x3 energy clusters give full muon energy containment. The increase between e3x3 and e5x5 is minimal. Figure 5.14. and Figure 5.15. show the average energy deposited by cosmic-ray muons as a function of of the seed tower. Here to avoid bias for border towers, we use e1x1 energy clusters. Figure 5.11. is particularly interesting for the BOTTOM wedge, configuration B. In this case, all four slices have approximately the same acceptance and angular coverage. Since the detector is completely symmetric in ϕ, the average energy deposited by cosmic-ray muons, should be proportional to the gain*qe (quantum efficiency) of the HPD used for that particular ϕ. For BOTTOM wedge, wedge 15, HB+ half-barrel, we observe a 30% change in average energy deposited by cosmic-ray muons, for $\phi = 55$ (spigot 11) vs $\phi = 58$ (spigot 14).

(a) Signal run. TOP: eta of seed tower candidate

(b) Signal run. BOTTOM: eta of seed tower candidate
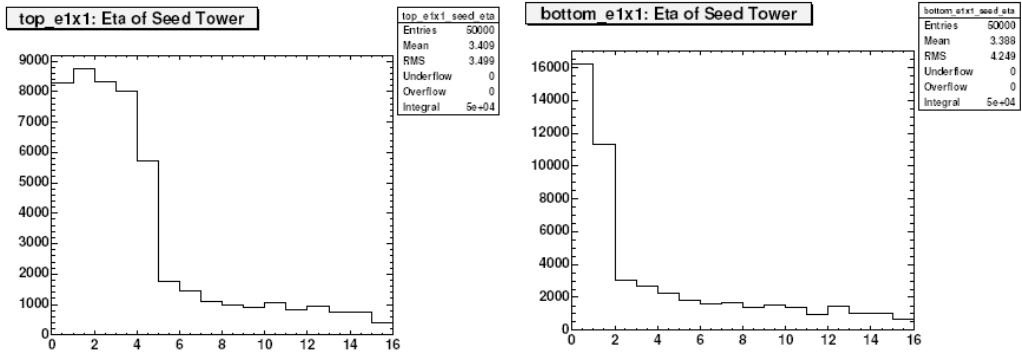
(c) Signal run. TOP: eta of seed tower candidate

(d) Signal run. BOTTOM: eta of seed tower candidate

(e) Background run. TOP: eta of seed tower candidate

(f) Background run. BOTTOM: eta of seed tower candidate

Figure 5.10.   Eta distribution for seed tower candidates. Signal run, config A: (a) TOP, (b) BOTTOM; Signal run, config B: (c) TOP, (d) BOTTOM; Background run: (e) TOP, (f) BOTTOM (Bakirci M.N. et al., 2007).
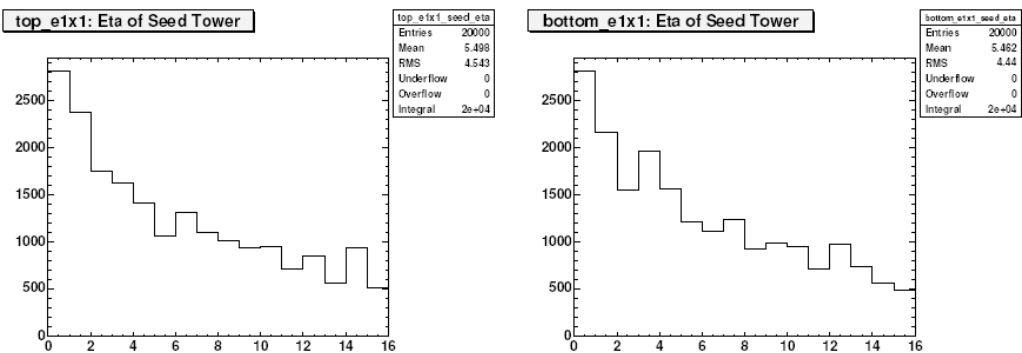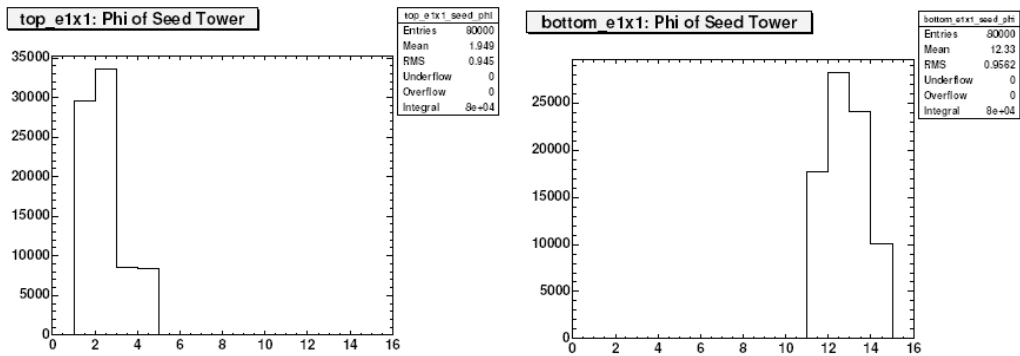
(a) Signal run. TOP: Phi of seed tower candidate

(b) Signal run. BOTTOM: Phi of seed tower candidate

(c) Signal run. TOP: Phi of seed tower candidate

(d) Signal run. BOTTOM: Phi of seed tower candidate

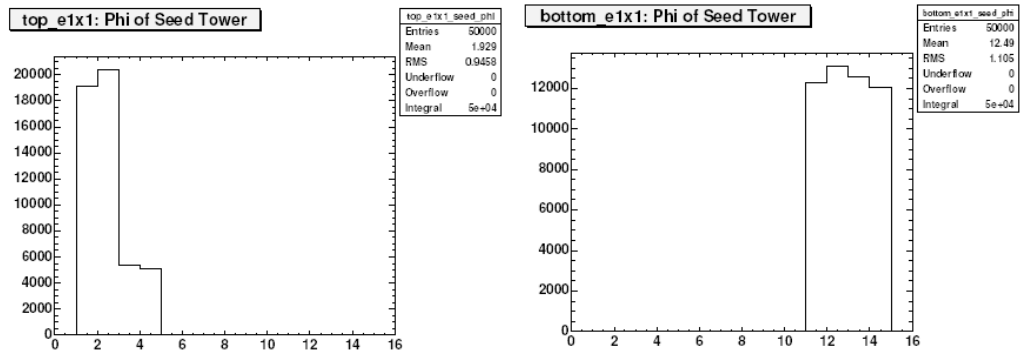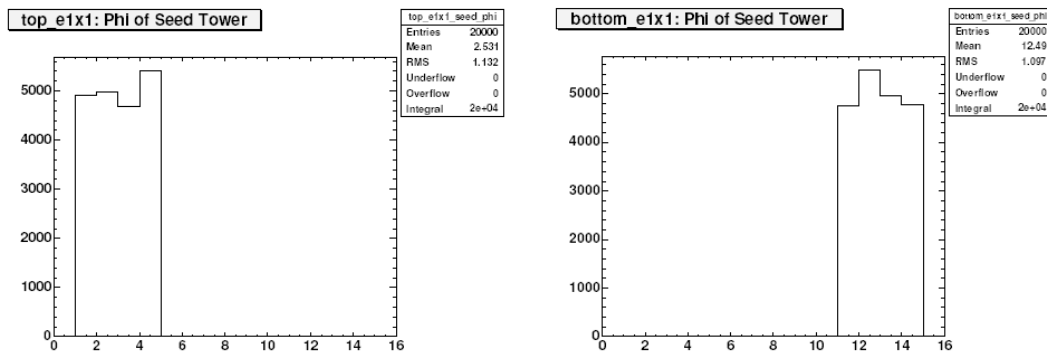(e) Background run. TOP: Phi of seed tower candidate

(f) Background run. BOTTOM: Phi of seed tower candidate

Figure 5.11.   Phi distribution for seed tower candidates. Signal run, config A: (a) TOP, (b) BOTTOM; Signal run, config B: (c) TOP, (d) BOTTOM; Background run: (e) TOP, (f) BOTTOM (Bakirci M.N. et al., 2007).
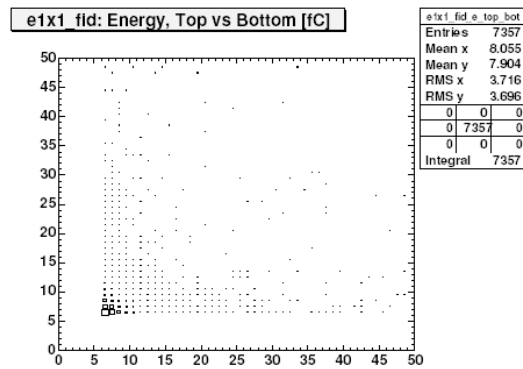
(a) 1x1 Cluster: TOP vs BOTTOM
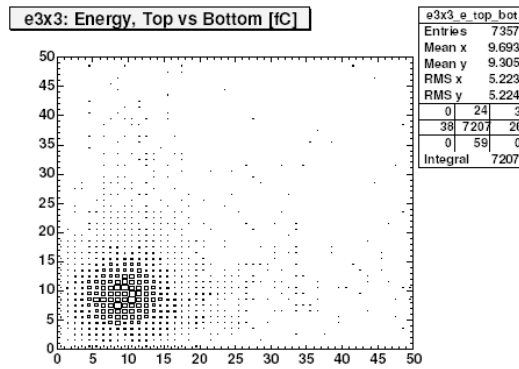
(b) 3x3 Cluster: TOP vs BOTTOM
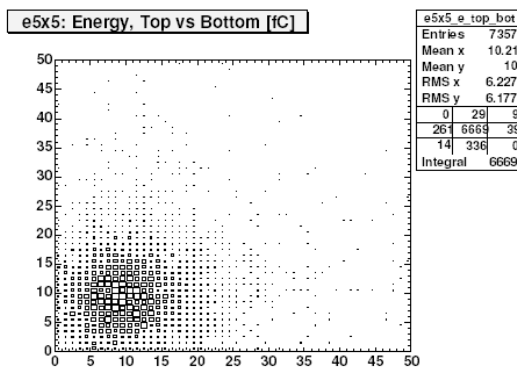
(c) 5x5 Cluster: TOP vs BOTTOM

Figure 5.12.   Configuration A: energy clusters e1x1, e3x3 and e5x5 of TOP vs BOTTOM wedge, for events passing 5 fC cuts. (a) 1x1 cluster, E(TOP) vs E(BOTTOM), (b) 3x3 cluster, E(TOP) vs E(BOTTOM), (c) 5x5 cluster, E(TOP) vs E(BOTTOM) (Bakirci M.N. et al., 2007).

Energy of Muon vs Cluster Size
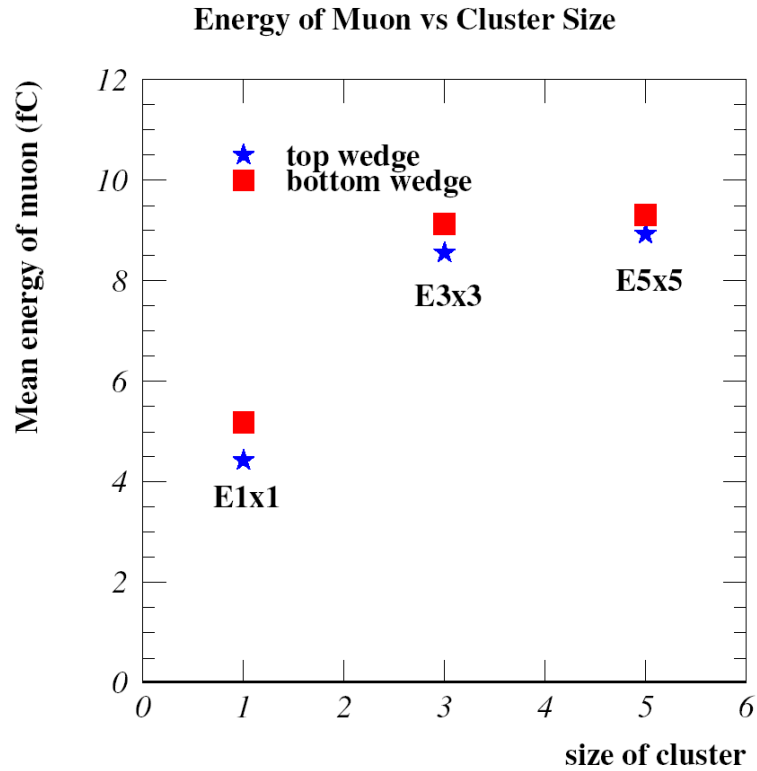
Figure 5.13.   Average cosmic-ray muon energy vs size of the energy cluster (e1x1, e3x3, e5x5) (Bakirci M.N. et al., 2007).
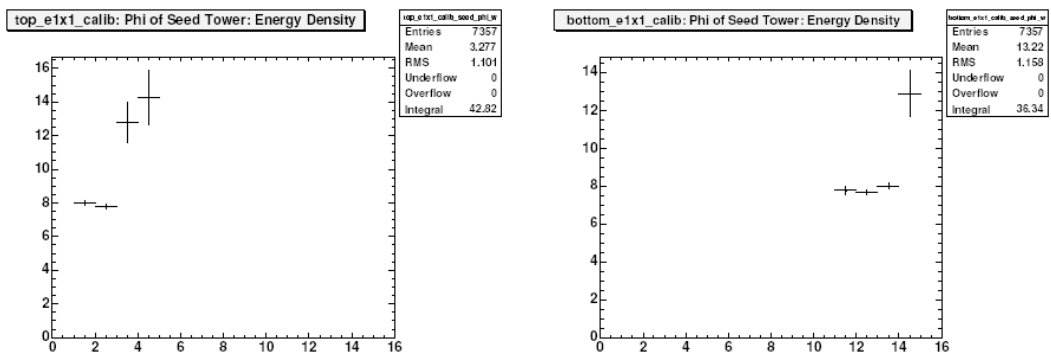
(a) Average energy of e1x1 cluster vs ϕ of the cluster: TOP

(b) Average energy of e1x1 cluster vs ϕ of the cluster: BOTTOM

Figure 5.14.   Average energy of e1x1 cluster vs ϕ of the cluster for configuration A, for TOP(a) and BOTTOM(b). We applied cut on the maximum energy of the seed tower E_{Seed} <50 fC. Errors are statistical, $dN/N = 1/\sqrt{N_{ENTRIES}}$ (See Figure 15) (Bakirci M.N. et al., 2007)
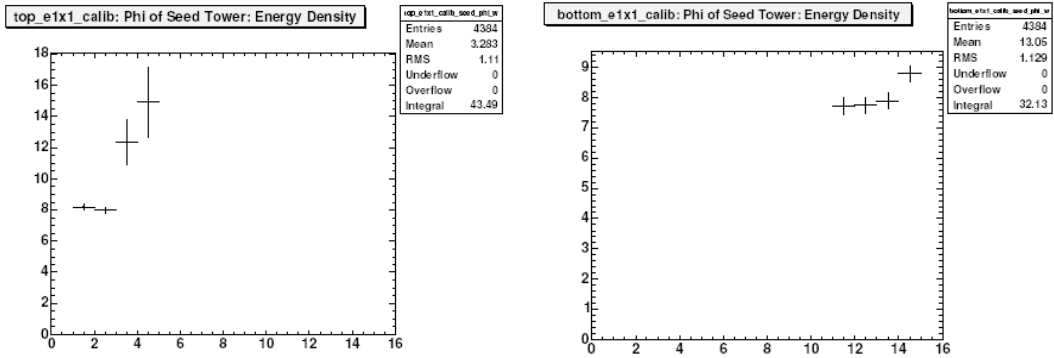
(a) Average energy of e1x1 cluster vs ϕ of the cluster: TOP

(b) Average energy of e1x1 cluster vs ϕ of the cluster: BOTTOM

Figure 5.15.   Average energy of e1x1 cluster vs ϕ of the cluster for configuration B, for TOP(a) and BOTTOM(b). We applied cut on the maximum energy of the seed tower E_{Seed} <50 fC. Errors are statistical, $dN/N = 1/\sqrt{N_{ENTRIES}}$ (See Figure 15) (Bakirci M.N. et al., 2007)

We have then compared the cosmic-muon results obtained with configuration B with measurement of HPD gains obtained with several different data sets: LED Burn-in and LED-QC and LED on-detector (HBP), wire source data, as well as HPD gain measurements done at University of Minnesota. The comparison is shown on Figure 5.16.. Four ϕ sectors of wedge 15 (ϕ= 55, 56, 57 and 58) show similar gain for LED Burn-in and LED-QC and LED on-detector (HBP) as well as wire source data.

Figure 5.16.   Comparison of HPD gains of four ϕ sectors of wedge 15 (ϕ= 55, 56, 57 and 58) with several different dat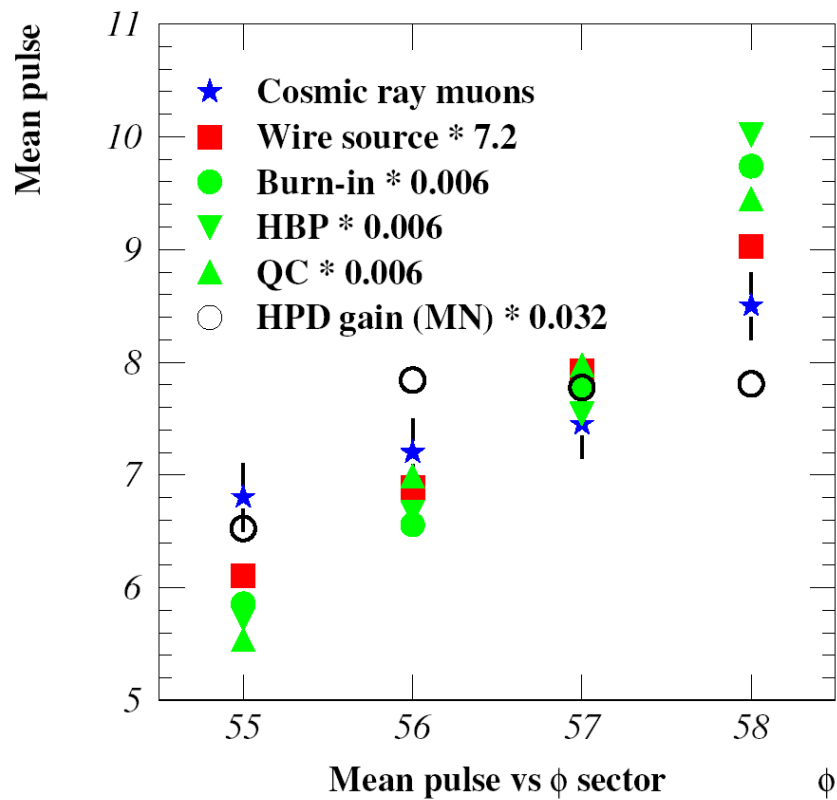a sets: cosmic-muons, LED Burn-in and LED-QC and LED on-detector (HBP), wire source data, as well as HPD gain measurements done at Univ. Minesota (Bakirci M.N. et al., 2007)

6. CONCLUSION

The gates beyond standard model will be opened when the CMS start taking data in fall 2009. Various parts of CMS detector need to be tested and understood before the LHC starts. In this thesis I present the analysis results of test beam data for CASTOR and HF RADDAM system as well as the SATOCRICH project which is the first sample of cosmic-ray events analysis for HCAL.

I presented the beam test data analysis for CASTOR calorimeter which is one of the very forward calorimeters of CMS. CASTOR is a quartz-tungsten sampling calorimeter based on Cherenkov light collection. Cherenkov light is converted to the signal by photodetectors which are a matrix of 4 or 6 Hamamatsu S8148 APDs. I studied the spatial response of EM part of CASTOR with 100 GeV electrons. The detector was scanned with the electrons horizontally and detector response versus beam impact points were studied. The derivative of the response is calculated and the electromagnetic shower width is found to be 1.7 mm. This result is consistent with the simulations with 1.56 mm shower width which was done using GEANT4 by Aslanoglu et. al.(Aslanoglu et. al., 2007a). Energy resolution of APDs are 2-3 times less than simulations (Aslanoglu et. al., 2007b). Additionally because of the harsh radiation environment in the forward region ($\sim$10-100MGy) and clear identification of the muon peak above pedestal and the large height of the HAD section and the limited space available for CASTOR calorimeter in very forward region, it was decided to use PMTs instead of APDs. The beam test results of CASTOR final prototype with PMTs can be found at (Aslanoglu et. al., 2008).

The radiation damage due to protons and damage recovery of HF calorimeter of CMS was also studied. The data was taken during beam test at IRRAD area of PS, in 2006 with irradiated 1m of 600 μm qp fiber. When $\sim$250 Mrad dose is accumulated the light transmission decreased to %33. At the end of the test when the beam was stopped the damage recovery was also calculated after one day and it was found that there is a $\sim$%50 increase in light transmission. That means that the response of calorimeter depends on the time the dose accumulated and this effect should taken into account when the calibration of the detector takes place when there is no LHC beam.

Since the cosmic-ray events are the most powerful source of data for CMS, I presented the analysis using cosmic-ray muons data for HCAL. This work is useful because one can

calibrate and test Hadron Calorimeter (HCAL) components and it helps improving our understanding of the detector. In the 5th chapter preliminary calibration of energy scale of two HCAL wedges using cosmic-ray muons is performed and compared with LED and wire-source data. We have measured time-of-flight of muons across a half-barrel, the result is consistent with speed of light, c=30 cm/ns ϕ sectors of wedge 15, HB+ half-barrel. We found that the relative calibration constants for these ϕ slices differ by up to 30%, implying that the gain of HPDs reading out those slices is different. We found a good agreement between relative calibration constants using average energy deposited by cosmic-ray muons with constants extracted using LED and wire source measurements.

REFERENCES

ABDULLIN S. et al., 2008. Design, performance, and calibration of CMS forward calorimeter wedges. Eur. Phys. J. C, 53, 139.

AKCHURIN N. and WIGMANS R., 2002. Review of Scientific Instruments. Vol74, No6.

AKCHURIN et al., 2002. Effects of radiation and their consequences for the performance of the forward calorimeters in the CMS experiment. Nucl. Inst. and Meth. in Phys. Res. B, 187, 66-78.

AKGUN U., 2003. Ph.D. thesis. University of Iowa.

ALBROW M. G., 2009. The FP420 R&D Project: Higgs and New Physics with forward protons at the LHC. arXiv:0806.0302.

ASLANOGLOU X. et al., 2007a. First performance studies of a prototype for the CASTOR forward calorimeter at the CMS experiment. arXiv:0706.2576v3.

ASLANOGLOU X., BAKIRCI M.N. and et al., 2007b. Performance studies of prototype II for the CASTOR forward calorimeter at the CMS experiment. Eur. Phys. J. C 52, 495-506.

ASLANOGLU X. et al., 2008. Performance studies of the final prototype for the CASTOR forward calorimeter at the CMS experiment. CMS NOTE-2008/022.

CASTOR EDR, 2007.

BAIATIAN et al., 2006. Design, Performance, and Calibration of CMS Forward Calorimeter Wedges. CMS NOTE-2006/044.

BAKIRCI M.N. et al., 2007. SATOCRICH Project: Special Assignment to Observe Cosmic Rays in CMS HCAL. CMS IN -2007/059.

BERARDI et al., 2004. TOTEM: Technical design report. Total cross section, elastic scattering and diffraction dissociation at the Large Hadron Collider at CERN. CERN-LHCC-2004-002.

BORRAS K., 2007. Status of Forward Physics Projects at CMS. Proceeds. DIS'07.

CANKOCAK K. et al., 2008. Radiation hardness measurements of high OH^- content quartz fibres irradiated with 24 GeV protons up to 1.25 Grad. Nucl. Inst. and Meth. in Phys. Res. A, 585, 2027.

CMS Collaboration, 2006. CMS Physics Technical Design Report Volume I: Detector Performance and Software, CERN/LHCC 2006-001.

_____, 1998. The Tracker Project Technical Design Report. CERN/LHCC 1998-006.

_____, 1997a. ECAL Technical Design Report. CERN/LHCC 1997-033

_____, 1997b. The Hadron Calorimeter Technical Design Report. CERN/LHCC 1997-031

_____, 1997c. The Magnet Project, Technical Design Report. CERN/LHCC 1997-10.

_____, 1997d. The Muon Project, Technical Design Report. CERN/LHCC 1997-32.

_____, 2000. Level-1 Trigger Technical Design Report. CERN/LHCC 2000-038.

_____, 2002. DAQ and High-Level Trigger Technical Design Report. CERN/LHCC 2002-026.

d'ENTERRIA D., 2008. Forward Physics at the LHC: within and beyond the Standard Model. Brazilian Journal of Physics, vol. 38, no. 3B.

DUMANOGLU I. et al., 2002. Radiation-hardness studies of high OH^- content quartz fibres irradiated with 500 MeV electrons. Nucl. Inst. and Meth. in Phys. Res. A, 490, 444-455.

GLASER M. et al., 1999. Nucl. Instr. and Meth. A 426, 72.

GRACHOV O. A. et al., 2006. Status of Zero Degree Calorimeter for CMS Experiment. arXiv:nucl-ex/0608052.

GRISCOM D.L. et al., 1993. Phys. Rev. Lett. 71, 1019.

HUHTINEN M. 1996. Ph.D. thesis. Helsinki University of Technology.

MANS J. and Fisher W., 2003. Data Acquisition Software for CMS HCAL Testbeams. arXiv:physics/0306093v1.

MERLO J. P., 2007. 10th ICATPP Conference On Astroparticle, Particle, Space Physics, Detectors And Medical Physics Applications. Conf. Proceedings, 575-579.

d'ROECK, 2006. Diffraction and Forward physics at the LHC. Czechoslovak Journal of physics, Vol. 56, Suppl. A.

ROYON C., 2007. Project to install roman pot detectors at 220 m in ATLAS. arXiv:0706.1796.

THOMAS R., 2004. MS thesis. Texas Tech University.

CURRICULUM VITAE

Name-Surname: Mustafa Numan BAKIRCI

Date of Birth: 20.03.1973

Place of Birth: Erzurum

Marital Status: Married

Contact: numan.bakirci@cern.ch

Educational Background

B.Sc.: Atatürk University, Faculty of Science&Letters, Department of Physics, Erzurum, 1995

M.Sc.: Çukurova University, Institute of Natural and Applied Sciences, Adana, 2003

Ph.D.: Çukurova University, Institute of Natural and Applied Sciences, Adana, 2009

Professional Experience

- **Physics Teacher** Bağlarbaşı Primary School, Şanlıurfa, 08/1995-01/1999

- **Research Assistant** Gaziosmanpaşa University, Faculty of Science&Letters, Department of Physics, Tokat, 02/1999-02/2000

- **Research Assistant** Çukurova University, Faculty of Science&Letters, Department of Physics, Adana, 02/2000-12/2009

- CMS HCAL Operataions Manager, CERN, 05/2009-.......